EES Batteries

REVIEW

View Article Online
View Journal

Cite this: DOI: 10.1039/d5eb00112a

Mn_3O_4 and its hybrids as anode active materials for lithium-ion batteries: a review

Lucy McElhone, [a,b] Peter C. Sherrell, [a,c] Andrew Thomas, [b,d] Aravind Vijayaraghavan [b,e] and Amanda V. Ellis *[a]

Received 12th June 2025,
Accepted 31st October 2025

DOI: 10.1039/d5eb00112a

rsc.li/EESBatteries

Developing new anode materials for lithium-ion batteries (LIBs) is of great interest to meet the rising global energy demand and requirements for electric vehicles (EVs). Manganese oxides (Mn_XO_Y) have high abundance, high theoretical specific capacities and are low in cost. This critical review provides a comprehensive literature review of Mn_XO_Y anodes, with particular emphasis on Mn_3O_4 and Mn_3O_4 hybrid materials. The evolution of the LIB is introduced, followed by problems with graphite anodes. Mn_XO_Y materials are discussed and the electrochemical testing, morphology and electrochemical performance of Mn_3O_4 and Mn_3O_4 hybrid anodes are compared in detail. Special attention has been paid to Mn_XO_Y/rGO anodes, examining synthesis methods, electrochemical properties, conversion mechanisms and ion diffusion rates. The future outlook and challenges in this field are also evaluated.

Broader context

Lithium-ion batteries (LIBs) have revolutionised energy storage, yet their anodes still typically rely on graphite. While providing key advantages in terms of stability and lifetime, graphite-anode LIBs remain limited by their low energy storage capability inherent to graphite. Next-generation LIBs need to possess high power density, high energy density, and exceptional stability, and thus the search for alternative anode materials that fulfil this requirement is critical. Manganese oxides have emerged as exciting alternative anode materials that may demonstrate this power, energy, and stability required for next-generation LIBs. However, the use of manganese oxide anodes is not well understood due to the variety of different manganese oxide stoichiometries (including MnO, Mn_3O_4, Mn_2O_3, MnO_2, Mn_2O_5, MnO_3, and Mn_2O_7), and a poor understanding of how lithium interacts with these different stoichiometries during LIB cycling. Herein, we systematically review the properties and LIB performance of manganese oxide stoichiometries, and explore strategies to mitigate their weaknesses, particularly by forming composites with other materials. By addressing key challenges and highlighting knowledge gaps, this review aims to position the research field to take full advantage of the properties of manganese oxide-based LIBs, towards high performance, next-generation LIBs.

1. Introduction

To date the most promising electrochemical energy storage device has been the lithium-ion battery (LIB). The journey of the LIB started in the 1970s when lithium (Li) metal was considered a prospective electrode material as a result of its electrochemical potential of −3.04 V compared to the standard hydrogen electrode (SHE).[1] Li has a small ionic radius leading to a high theoretical gravimetric capacity (3860 mAh g^{-1}).[2] It is also the third lightest element and has low density (0.53 g cm^{-3}) and low molar mass (6.94 g mol^{-1}) which are desirable properties for batteries in electric vehicles (EVs).[1] In 1976, Whittingham[3] developed the first rechargeable LIB using a Li metal anode, titanium disulphide (TiS_2) cathode and lithium perchlorate ($LiClO_4$) in dioxolane electrolyte. The system relied on intercalation, in which Li^+ ions were inserted into the layered structure of TiS_2.[1] However, upon repeated charging and discharging, Li metal dendrites grew on the Li metal anode, resulting in a build-up of dead Li, causing internal short circuits.[2] A further concern was that Li metal is highly reactive, leading to fires and explosions.[1,2,4,5]

In 1979, Basu *et al.*[6] replaced the Li metal anode with graphite. In this system, Li^+ ions intercalated into graphite during charging and into a niobium triselenide ($NbSe_3$) cathode during discharging.[6] In 1980, Godshall *et al.*[7] at Stanford University and Goodenough *et al.*[8] at Oxford University independently used a lithium cobalt oxide ($LiCoO_2$) cathode. This new cathode material laid the foundation for modern LIBs.

In 1985, Yoshino[5] designed the first prototype LIB, with a graphite anode and a $LiCoO_2$ cathode. This dramatically

[a]Department of Chemical Engineering, The University of Melbourne, Parkville, Victoria, 3010, Australia. E-mail: amanda.ellis@unimelb.edu.au
[b]Department of Materials, The University of Manchester, Booth St East, Manchester, M13 9PL, UK
[c]School of Science, RMIT University, Victoria 3001, Australia
[d]The Photon Science Institute, The University of Manchester, Wilton Street, Manchester, M13 9PL, UK
[e]The National Graphene Institute, The University of Manchester, Booth St East, Manchester, M13 9PL, UK

improved the safety of LIBs,[4,5] and led to Sony releasing the first commercial LIB in 1991.[9] In 2019, Whittingham, Goodenough and Yoshino were awarded the Nobel Prize in Chemistry for their work on LIBs.[10]

Graphite is today widely used as an anode material in commercial LIBs as it is low in cost,[11] has stable electrochemical performance[11] and a low lithiation/delithiation potential (0.01–0.2 V *vs.* Li/Li^+ for natural graphite).[12] However, there is a need to develop alternative anode materials due to the following concerns.

Natural graphite anodes have a limited specific capacity of 372 mAh g^{-1}.[13,14] This is because they rely on an intercalation mechanism involving the lithiation or delithiation of Li^+ ions into and out of the graphene sheets that make up the graphite crystalline lattice.[15] There are, therefore, a limited number of sites in which Li^+ ions can insert or de-insert.[16] Moreover, this mechanism has sluggish kinetics[11] due to the slow intrinsic diffusivity of the Li^+ ion in graphite (10^{-8} cm^2 s^{-1}).[17]

Another issue is the instability of the solid electrolyte interface (SEI) layer in graphite anodes.[12] During the first few charge–discharge cycles (formation cycles), the electrolyte decomposes to form a SEI layer on the graphite surface.[18] The SEI layer consists of Li^+ ions, salts, impurities and reduced solvents from the electrolyte.[15] In theory, the SEI layer stops electrolyte degradation and protects the anode because it is ionically conductive (allows movement of Li^+ ions) but, at the same time, electrically insulating (it does not allow movement of electrons).[19] However, volume changes of 9% can occur during cycling.[12] This means that the SEI layer formed on natural graphite can have poor mechanical strength and potentially crack.[20] More of the graphite surface therefore becomes exposed, resulting in continuous electrolyte decomposition[12] and undesirable thickening of the SEI layer, giving low capacity and cyclability.[18]

A third issue is that graphite anodes are not suitable for fast charging.[11] At the high C-rates (above 1C) required for fast charging,[21] Li metal plating of the graphite surface, as well as Li dendrite growth can occur, both of which often lead to failure of the device.[12] Furthermore, the speed of lithium ion diffusion in graphite greatly varies.[21] Graphite consists of layers of graphene. Although diffusion rates can be fast (10^{-6} cm^2 s^{-1}) parallel to the graphene planes,[22] they are slow (10^{-12} cm^2 s^{-1}) perpendicular to the graphene planes.[21] Due to the slow kinetics of Li intercalation into graphite, polarisation can occur during fast charging.[11] As graphite has a low lithiation/delithiation potential (0.01–0.2 V *vs.* Li/Li^+)[12] this polarisation can cause the operating voltage to drop to below 0 V *vs.* Li/Li^+, further accelerating Li plating.[11] The build-up of Li leads to a rapid fade in capacity and is also a safety concern, leading to internal short circuits and thermal runaway.[11] Graphite anodes are therefore modified to improve the fast charging capability for electric vehicles. Approaches include etching to create pores,[23] employing nitrile solvents and aliphatic esters with low viscosity to enhance ionic conductivity,[24] developing new electrolytes to reduce the desolvation energy of Li^+ and create a robust SEI layer,[25] and blending with silicon oxide.[26] However, further work is needed.

Finally, the environmental impact of producing graphite must be considered. There are two main types of graphite – natural and synthetic. 1.1×10^4 MJ of energy is consumed when producing 1 ton of natural graphite,[12] whereas for synthetic graphite this value is higher (4.0×10^4 MJ).[12] Production of synthetic graphite is a highly energy intensive process as it requires heating carbon precursors to 4000 °C for long periods of time.[27] On the other hand, natural graphite cannot be used before processing as it contains impurities. It must be processed to battery grade graphite which has a carbon content of greater than 99.5%.[28] This involves environmentally unfriendly, highly toxic and corrosive reagents such as hydrogen fluoride.[29] In 2015, the Paris Agreement predicted that 100 million electric vehicles will be on the roads by 2030.[30] Given that 1 LIB for 1 EV contains 75–115 kg of graphite[27,30] the demand for graphite will increase and LIBs may become more expensive to build.[9] Several reviews discuss the advantages and challenges of graphite anodes in LIBs in detail.[1,4,11,12,16,31]

Thus, there is a clear need to investigate alternative anode materials which are more sustainable, environmentally friendly and processable, whilst also offering higher capacities and higher energy densities than graphite.

There has been a concerted shift in LIB research away from intercalation anodes like graphite towards alloying- and conversion-type anodes. Alloying-type anode have attracted great interest due to their high theoretical capacities (over 3000 mAh g^{-1}).[32] However, examples such as silicon (Si), germanium (Ge) and tin (Sn) suffer from large volumetric expansion during lithiation/delithiation of approximately 270%,[32] 255%[14] and 240%[14] respectively, leading to pulverisation and rapid capacity decay during cycling.[16] Phosphorus (P) based anodes also have a high theoretical capacity of up to 2596 mAh g^{-1}, however, like Si, they suffer from large volumetric expansion of approximately 216%,[33] resulting in poor cycle stability. Other issues include phosphorus's tendency to self-oxidise, the slow kinetics of the alloying reaction[33] and the potential to form phosphine which is toxic.[14]

On the other hand, conversion-type anodes are a promising alternative. They undergo a conversion mechanism involving multiple multivalent redox reactions with a series of bond-breaking and bond-making steps.[34,35] These materials include transition metal oxides (TMOs),[36] selenides,[37] phosphides[38] and dichalcogenides.[39] Importantly, they are low in cost and have higher theoretical capacities (500–1500 mAh g^{-1})[35] than that of graphite (372 mAh g^{-1}).[35]

In particular, TMOs have attracted great interest since the early 2000s,[40] with the conversion-type mechanism describe d in reaction (1),[41] where M represents a transition metal

$$M_XO_y + 2y\,Li^+ + 2y\,e^- \underset{\text{<- Discharging}}{\overset{\text{Charging ->}}{\leftrightarrow}} xM^0 + yLi_2O \quad (1)$$

.

Here, in contrast to intercalation, $2y$ times more Li^+ ions can be stored per formula unit.[41] During charging, transition

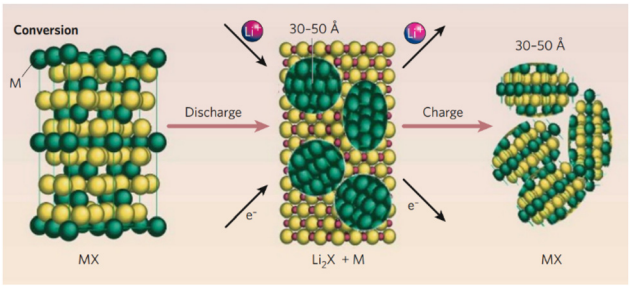

Fig. 1 A schematic showing the conversion mechanism. Reproduced with permission.[9] Copyright 2008, Springer Nature.

metal clusters form and embed into lithium oxide (Li_2O)[41] then upon discharging, oxidation of the clusters occurs, forming amorphous TMO[41] as shown in Fig. 1.

Emerging conversion-type TMO anodes are those fabricated from manganese oxides and manganese oxide hybrid materials.[42] Manganese is highly abundant[43] and found in ores across the world in countries such as South Africa, Brazil, Australia and Ukraine.[44] Manganese oxides possess several advantages compared to other TMOs as LIB anode materials, such as high specific capacities (756–1223 mAh g^{-1}),[41] low toxicity, low cost[45] and a low reaction potential (0.2–0.5 V) during the first discharge cycle.[46,47] However, like many TMOs manganese oxides suffer from low electronic conductivity,[48] for example, 10^{-7}–10^{-8} S m^{-1} for Mn_3O_4.[45] As conversion anodes, they also exhibit a large coulombic inefficiency in the first cycle due to formation of the SEI layer and some volume changes during cycling.[45]

Different strategies have been introduced to relieve these problems. Manganese oxide nano- and micro-structures have been fabricated to increase the surface area and reduce volume changes during cycling.[42] Manganese oxides have also been combined with conductive carbon materials by carbon coating or hybridising with materials such as reduced graphene oxide (rGO). rGO has a large surface area, high conductivity, chemical stability, low density and excellent mechanical strength.[49,50]

Therefore, this review will focus on current research into the replacement of the graphite anode in LIBs with manganese oxide and manganese oxide hybrid materials. While several reviews have discussed TMO and Mn-based anodes,[40,45] they primarily summarise early work and do not reflect the rapid developments or emerging focus on Mn_3O_4 and Mn_3O_4/rGO anodes over the past decade. This review therefore provides an up-to-date review of Mn_3O_4, carbon-coated Mn_3O_4, Mn_3O_4/graphene and Mn_3O_4/rGO anodes for LIBs. This review pays particular attention to Mn_3O_4/rGO anodes which show promising high capacities, offering new insights into their conversion mechanisms. Synthesis methods for Mn_XO_Y anodes, electrochemical properties and ion diffusion rates for Mn_3O_4/rGO are reviewed. The key challenges and outlook for Mn_3O_4, Mn_3O_4 hybrid and Mn_3O_4/rGO anodes are also discussed.

2. Manganese oxide anodes for LIBs

2.1 Manganese oxides

Manganese oxides are environmentally friendly, inexpensive, highly abundant and provide excellent safety for LIBs. Manganese has seven common oxidation states (Table 1) with multiple different crystal structures,[51] some of which are useful for charge storage. They also have various morphologies and porosity, providing a range of electrochemical properties.[52] The most stable oxidation states are +2, +3 and +4.[53] Oxidation states of +5, +6 and +7 are less stable and not explored as energy storage materials.[54] Manganese(v) oxide, Mn_2O_5, is not stable at all.[54] Manganese(vi) oxide, MnO_3, does appear to exist[54] as a stable compound and manganese(vi) salts have been prepared[53] in the form of sodium manganate, $Na_{0.7}MnO_{2.05}$,[55] and potassium manganate,[54] K_2MnO_4. Manganese(vii) oxide, Mn_2O_7, is explosive, however useful salts in the +7 oxidation state such as lithium permanganate,[56] $LiMnO_4$, and potassium permanganate, $KMnO_4$ are well known.[54] This review will, therefore, focus on current manganese oxide anode materials for LIBs, including MnO_2, Mn_3O_4 and Mn_3O_4 hybrid anodes.

2.2 Electrochemical testing

This section reviews the electrochemical testing of manganese oxide anodes in the literature. Firstly, the structure of the coin

Table 1 Different oxides of manganese, their crystal structures and capacities

Formula	Oxidation state of Mn	Crystal structures	Theoretical specific capacity[a] (mAh g^{-1})
MnO	+2	Cubic rock salt[41]	756[41]
Mn_3O_4	+2, +3	Hausmannite (spinel)[89]	937[41]
Mn_2O_3	+3	Cubic bixbyite (α),[90] orthorhomic bixbyite (β),[91] spinel-like (γ),[92] rhombohedral imenite (ε),[93] perovskite-like (ζ)[91]	1019[41]
MnO_2	+4	Various polymorphs including pyrolusite (β),[94] ramsdellite (R),[95] hollandite (α),[96] intergrowth (γ),[97] spinel (λ),[98] layered (δ)[99] and non-degenerate perovskite[100]	1223[41]
Mn_2O_5	+5	Not used as LIB anode	
MnO_3	+6	Not used as LIB anode	
Mn_2O_7	+7	Not used as LIB anode	

[a] Numbered subscripts indicate references.

cell set-up for testing is explained, followed by a comparison of various factors including active material, working electrode composition, electrolyte and solvent.

2.2.1 Cell components. Current literature reports electrochemical testing of manganese oxide-type electrodes for LIBs primarily in half-cell configurations, with a limited number of studies on full-cells.[57–59] In the half cell configuration, the working electrode is the manganese oxide anode, and the counter electrode is lithium metal, all in an electrolyte, with a separator in-between the two electrodes, as illustrated in Fig. 2. The working electrode (anode) consists of three components: active material (manganese oxide or manganese oxide hybrid), conductive additive, and binder. The conductive additive is usually acetylene black or carbon black (Super P). The binder is often polyvinylidene difluoride (PVDF)[60–73] in *N*-methyl pyrrolidone (NMP). Other binders have been used such as carboxymethyl cellulose (CMC),[59,74–83] polytetrafluoroethylene (PTFE),[84] sodium alginate[85] and polyacrylic acid (PAA).[86–88] The binder, conductive additive and active material are mixed and coated onto copper (Cu) foil which acts as a current collector.

An important factor is the mass loading of the active material on the Cu foil current collector. In general, this is around 1 mg cm^{-2} for half-cell anodes, however, it is often not reported in literature. The potential range for electrochemical testing is usually between 0.01 V and 3 V *vs.* Li/Li^+. The preferred electrolyte in the cell is lithium hexafluorophosphate ($LiPF_6$) in two or more organic solvents in a 1 : 1 volume ratio. These solvents are often dimethyl carbonate (DMC), diethyl carbonate (DEC) or ethyl methyl carbonate (EMC). Sometimes 3–10% of fluoroethylene carbonate (FEC)[72,79,88] or vinylene carbonate (VC)[66] is added to promote formation of a stable solid electrolyte interface (SEI) layer at the Li metal/electrolyte interface and improve capacity retention.[101] However, the detailed effects of these additives on SEI composition remain poorly understood for Mn-oxide anodes. A separator consisting of a polypropylene membrane, such as Celgard, is used to allow Li^+ ions to pass through and the counter electrode (Co.E) and reference electrode (Ref.E) is usually lithium metal. Table 2 summarises recent materials that have shown promise as active materials as conversion-type anodes in LIBs. Their respective working electrode, mass ratios of active material : conductive carbon : binder and binder type are specified, along with voltage ranges, mass loadings, electrolyte and separator type used in half-cell testing.

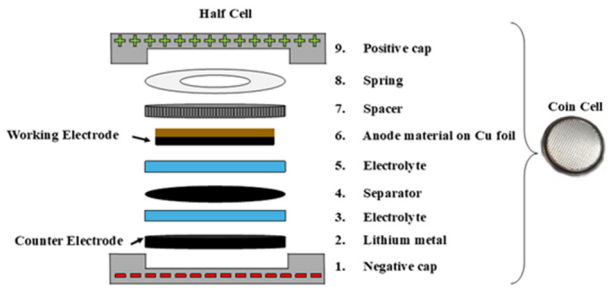

Fig. 2 Components of the half-cell. Right: finished coin cell.

2.3. MnO_2 anodes for LIBs

Over the past decade, MnO_2 has been explored as an LIB anode material.[111–114] This interest stems from its promising theoretical specific capacity (up to 1223 mAh g^{-1})[41] and high abundance, with pyrolusite being the most common manganese ore.[54] In reality, this high specific capacity is not often reached as MnO_2 in its natural form has a low Li^+ diffusion constant (10^{-13} cm^2 V s^{-1}), poor structural stability and poor electrical conductivity (10^{-5}–10^{-6} S cm^{-1}).[115] Researchers have endeavoured to improve the capacity in various ways including creating urchin-like morphologies,[113,116] nanorod composites with rGO[117,118] and doping with other atoms.[114] Despite this, researchers have found that MnO_2 is less promising for future LIB anode research and consequently the research has shifted towards other Mn oxide materials, including Mn_3O_4.

2.4 Mn_3O_4 and Mn_3O_4 hybrid anodes for LIBs

The following sections discuss the more promising LIB anodes, *i.e.* Mn_3O_4 and Mn_3O_4 hybrid anodes. Their properties are compared including, morphology, diameter and initial discharge specific capacity. Also discussed is the reversible capacity – the capacity retained after a specific number of charge/discharge cycles – at a given current density, and the capacity retention (%). Finally, if mentioned in the literature, the coulombic efficiency (C.E.) (eqn (1)) will be noted.[119]

$$\text{C.E.} = \frac{\text{discharge capacity}}{\text{charge capacity}} \quad (1)$$

In recent years, Mn_3O_4 has attracted significant interest as an LIB anode material. The average charge and discharge potentials of Mn_3O_4 compared to Li/Li^+ are 0.5 V and 1.5 V, which are low compared to other materials, for example, Fe_3O_4.[80,87] Using Mn_3O_4 anodes therefore increases the working voltage and therefore, energy density, when paired with commercial cathodes.[77] It also has specific advantages compared to other manganese oxides. For instance, Mn_3O_4 has a lower voltage hysteresis (<0.8 V) than that of MnO_2 and a higher theoretical capacity (936 mAh g^{-1})[105] compared to that of MnO (756 mAh g^1).[42]

Li *et al.*[120] reported that the superior attributes of Mn_3O_4, as a LIB anode active material, compared to Mn_2O_3 were due to its spinel structure (Fig. 3), where Mn^{2+} ions occupy tetrahedral sites and Mn^{3+} ions occupy octahedral sites.[51,62] The tightly combined octahedral and tetrahedral sites, along with cubic close packing of the oxide anions, minimises repulsion between like-charges, resulting in a thermodynamically stable structure.[121] Mn_3O_4 anodes do, however, have poor electronic conductivity (10^{-7}–10^{-8} S m^{-1}) and slow ion diffusion rates.[42,67,107,122]

These issues have been addressed in several ways. Firstly, by designing new micro- and nano-sized structures including nanoflowers,[76] nanoparticles,[42,65,66,80,81,102,105,106,109,123]

Table 2 Components of coin cells and potential ranges for Mn_3O_4, Mn_3O_4/TMOs, fluorinated Mn_3O_4, carbon-coated Mn_3O_4, Mn_3O_4/graphene and Mn_3O_4/rGO anodes in the literature. Note that these are all half-cells

Active material	Working electrode (mass ratios)	Potential Range *vs.* Li/Li^+ (V)	Mass loading[a]	Electrolyte in solvent (v/v) and separator	Ref.E.	Co.E	Year	Ref.
Mn_3O_4	AM, carbon black, PVDF 7 : 2 : 1	—	—	1 M $LiPF_6$ in EC : DMC 1 : 1	—	Li foil	2014	102
Mn_3O_4 porous nanorods	AM, acetylene black, CMC 7 : 2 : 1	0.01–3 V	—	1 M $LiPF_6$ in EC/DMC/EMC 1 : 1 : 1, Celgard 2400	—		2014	74
Mn_3O_4 microspheres	AM, carbon black, sodium CMC 7 : 2 : 1	0.01–3 V	1.5 mg cm^{-2}	1 M $LiPF_6$ in EC/DMC/EMC 1 : 1 : 1, Celgard 2400	—	Li foil	2015	59
Mn_3O_4 nanowires	AM, carbon black, PVDF/NMP 8 : 1 : 1	0.01–3 V	1.5 mg cm^{-2}	—	—	—	2015	61
Mn_3O_4 nanosheets	AM, acetylene black, PTFE 8 : 1 : 1	0.01–3 V	2 mg	1 M $LiPF_6$ in EC/DMC/EMC 1 : 1 : 1	Li metal	Li metal	2016	84
Mn_3O_4 microspheres	AM, acetylene black, PVDF 7 : 2 : 1 in NMP	0.01–3 V	—	1 M $LiPF_6$ in EC/DMC 1 : 1, Celgard 2300	Li foil	Li foil	2017	73
Mn_3O_4 microplates	AM, carbon black, CMC 7 : 2 : 1	0.01–3 V	1 mg cm^{-2}	1 M $LiPF_6$ in EC/DMC 1 : 1	Li metal	Li metal	2017	77
Mn_3O_4 nanowires	AM, Super P, PVDF 70 : 15 : 15 in NMP	0.005–3 V	1–2 mg cm^{-2}	1 M $LiPF_6$ in EC/DMC/DEC 1 : 1 : 1	—	Li metal	2019	69
2D Mn_3O_4 nanosheets	AM, Super P, PVDF 7 : 2 : 1 in NMP	0.01–3 V	—	1 M $LiPF_6$ in EC/DEC 1 : 1 and 3% FEC	—	—	2019	72
Mn_3O_4 nano-octahedrons	AM, carbon black, PVDF 7 : 2 : 1 in NMP	0.01–3 V	—	1 M $LiPF_6$, Celgard 2400	—	Li metal	2020	68
Mn_3O_4	AM, carbon black, CMC 7 : 2 : 1	0.01–3 V	—	1 M $LiPF_6$ in EC : DEC 1 : 1, Celgard 2250	—	Li metal	2022	81
Hydrogenated TiO_2-coated Mn_3O_4	AM, carbon black, CMC 7 : 2 : 1	0.01–3 V	1–2 mg cm^{-2}	1 M $LiPF_6$ in EC/DEC/DMC 1 : 1 : 1, Celgard 2400	Li foil	Li foil	2015	75
Mn_3O_4/Fe_3O_4	AM, acetylene black, CMC 6 : 2 : 2 in H_2O	0.01–3 V	1–2 mg cm^{-2}	1 M $LiPF_6$ in EC/DMC/EMC 1 : 1 : 1, Celgard 2300	—	—	2015	76
Fluorinated Mn_3O_4 nanospheres	AM, Super P, PVDF 70 : 15 : 15 in NMP	0.005–3 V	1.5–2 mg cm^{-2}	1 M $LiPF_6$ in EC/DEC/DMC 1 : 1 : 1	—	Li metal	2018	64
ZnO/Mn_3O_4 nanospheres	AM, acetylene black, CMC 6 : 2 : 2	0.01–3 V	—	1 M $LiPF_6$ in EC/DEC/DMC 1 : 1 : 1 +5% FEC	—	—	2020	79
Mn_3O_4 on Fe_2O_3 micro discs	AM, acetylene black, CMC 7 : 2 : 1	0.01–3 V	—	1M $LiPF_6$ in EC : DMC 1 : 1, polypropylene film	—	Li metal	2023	82
Mn_3O_4 carbon microspheres	AM, Super P, PVDF 8 : 1 : 1	0.01–3 V	—	1 M $LiPF_6$ in EC/DMC 1 : 1	Li pellet	Li pellet	2015	103
Mesoporous Mn_3O_4/C microspheres	AM, acetylene black, PVDF 7 : 2 : 1 in NMP	0.01–3 V	1 mg cm^{-2}	1 M $LiPF_6$ in EMC/DEC/EC 1 : 1 : 1, Celgard 2400	Li foil	Li foil	2017	63
Mn_3O_4 on exfoliated graphite	AM, acetylene black, PVDF 8 : 1 : 1 in NMP	0.05–3 V	1.16 mg cm^{-2}	1 M $LiPF_6$ in EC/DMC 1 : 1 +5% VC, Celgard 2400	Li metal	—	2017	66
Mn_3O_4@C micro/nanocuboids	AM, Super P, PAA 8 : 1 : 1 in NMP	–3 V	1–1.1 mg cm^{-2}	1 M $LiPF_6$ in EC/DEC 1 : 1	—	Li metal	2018	87
Carbon-coated Mn_3O_4 nanospheres	AM, Super P, PAA 75 : 15 : 15 in NMP	0.005–3 V	0.6 mg cm^{-2}	1 M $LiPF_6$ in EC/DEC 1 : 1 and 10% FEC	—	Li foil	2018	88
Carbon-coated Mn_3O_4 microspheres	AM, carbon black, PVDF 8 : 1 : 1 in NMP	0.01–3 V	1.23 mg cm^{-2}	1 M $LiPF_6$ in EC/DEC 1 : 1	—	Li foil	2019	70
Mn_3O_4 on N-doped porous C	AM, acetylene black, PVDF 8 : 1 : 1 in NMP	0.01–3 V	2 mg	1 M $LiPF_6$ in EC/DMC/DEC 1 : 1 : 1, Celgard 2400	—	Li foil	2018	65
N-doped carbon Mn_3O_4 microspheres	AM, acetylene black, PVDF 8 : 2 : 2	0.01–3 V	—	1 M $LiPF_6$ in EC/DEC 1 : 1, polypropylene membrane	—	Li foil	2020	104
Mn_3O_4 on carbon nanotubes	AM, Super P, sodium CMC 85 : 5 : 10	—	—	1 M $LiPF_6$ in EC/DMC 1 : 1, Celgard 2320	Li foil	Li foil	2021	80
Mn_3O_4/C nanosheet	AM, Super P, PVDF 8 : 1 : 1	0.01–3 V	0.8–1.1 mg	1 M $LiPF_6$ in EC : DMC 1 : 1, Celgard 2400	—	Li foil	2024	42
Mn_3O_4/graphene nanosheet	AM, carbon black, PVDF 8 : 1 : 1	0.1–3 V	2.0 mg cm^{-2}	1 M $LiPF_6$ in EC : DEC 1 : 1	—	Li foil	2010	50
Mn_3O_4/graphene nanosheet	AM, Super P, PVDF 8 : 1 : 1	0.01–3 V	0.9 mg	1 M $LiPF_6$ in EC : DEC 1 : 1	—	Li foil	2013	105
Mn_3O_4 nanorods on graphene nanosheet	AM, acetylene black, sodium alginate 7 : 2 : 1	0.01–3 V	—	1 M $LiPF_6$, Celgard 2500	—	—	2017	85
Mn_3O_4 on graphene nanosheets	AM, NMP 90 : 10	0.01–3 V	—	1 M $LiPF_6$ in EC/DEC 1 : 1, Celgard 2250	—	Li foil	2018	106
Mn_3O_4/graphene	AM, Super P, CMC 7 : 2 : 1 in citric acid	0–2 V	1.2 mg cm^{-2}	1 M $LiPF_6$ in EC/DMC 1 : 1, Whatman GF/D glass microfiber sheet	—	Li foil	2019	78
Graphene-coated carbon-coated Mn_3O_4	AM, carbon black, PVDF 8 : 1 : 1 in NMP	0.01–3 V	2 mg cm^{-2}	1 M $LiPF_6$ in EC/DMC 1 : 1, glass microfibre separator	—	Li foil on Ni plate	2021	71

Table 2 *(Contd.)*

Active material	Working electrode (mass ratios)	Potential Range *vs.* Li/Li^+ (V)	Mass loading[a]	Electrolyte in solvent (v/v) and separator	Ref.E.	Co.E	Year	Ref.
Mn_3O_4/graphene	Binder-free method	0.01–3 V	0.8 mg cm^{-2}	1 M $LiPF_6$ in EC : DEC 1 : 1, Celgard 2400	—	Pt foil	2022	107
Graphene-wrapped $MnCO_3/Mn_3O_4$	AM, Super P, PVDF 8 : 1 : 1 in NMP	0.01–3 V	—	1 M $LiPF_6$ in EC : DEC 1 : 1	—	Li foil	2022	67
Mn_3O_4 in N-doped graphene	AM, acetylene black, PVDF 75 : 15 : 10 in NMP	0.01–3 V	2 mg cm^{-2}	1 M $LiPF_6$ in EC : DEC 1 : 1, Celgard 2500	Li metal	—	2023	62
Porous Mn_3O_4 nanorod/rGO hybrid paper	No binder or conductive additive	0.05–3 V	—	1 M $LiPF_6$ in EC/DMC 1 : 1	—	—	2016	108
Acid-treated rGO/ Mn_3O_4 nanorod	AM, Super P, PVDF 7 : 2 : 1 in NMP	0.01–3 V	—	1 M $LiPF_6$ in EC/DMC 1 : 1	—	—	2017	60
Mn_3O_4 in 3D rGO	No binder or additive, details not given	0.01–3 V	—	1 M $LiPF_6$ in EC/DMC/EMC 1 : 1 : 1, Celgard 2400	Li foil		2017	109
Mn_3O_4/rGO	AM, Super P, LiOH, PAA 80 : 10 : 5 : 5	0.002–3 V	—	1 M $LiPF_6$ in EC/DEC 1 : 1	—	Li foil	2020	86
Mn_3O_4/rGO	AM, carbon black, PVDF 8 : 1 : 1	—	—	1 M $LiPF_6$ in EC : DMC 1 : 1	—	—	2022	110

AM = active material. Ref.E = reference electrode. Co.E = counter electrode. Abbreviations for chemicals are as follows: CMC = carboxymethyl cellulose, DEC = diethyl carbonate, DMC = dimethyl carbonate, EC = ethylene carbonate, EMC = ethyl methyl carbonate, FEC = fluoroethylene carbonate, NMP = *N*-methyl pyrrolidone, PAA = polyacrylic acid, PTFE = polytetrafluoroethylene, PVDF = polyvinylidene difluoride, VC = vinylene carbonate. [a] Mass loading values are reported in mg cm^{-2}, or in mg when the electrode area was not specified in the source.

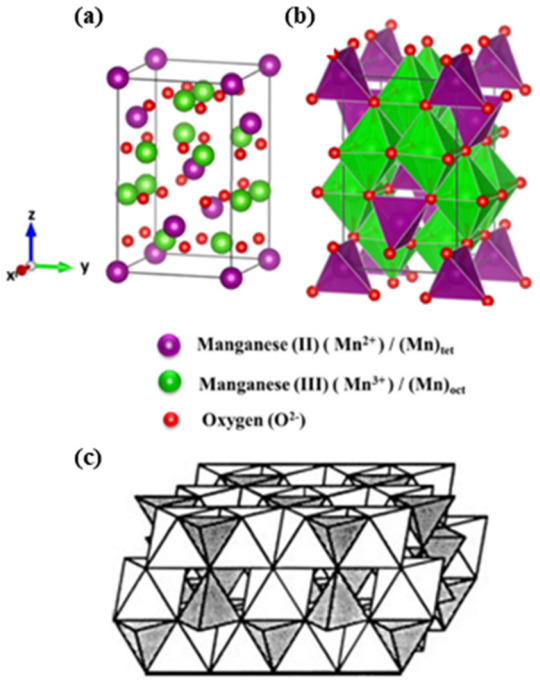

Fig. 3 Structural models of Mn_3O_4 (a) arrangement of atoms in one unit cell and (b) arrangement of tetrahedra and octahedra in one unit cell. Reproduced with permission.[118] Copyright 2018, Springer Nature. (c) Spinel type structure consisting of MnO_6 octahedra (white) and MnO_4 tetrahedra (grey). Reproduced with permission.[51] Copyright 2011, John Wiley and Sons.

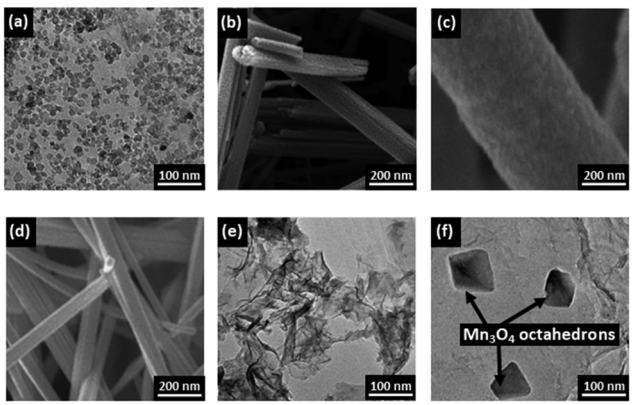

Fig. 4 Morphologies of Mn_3O_4 anodes. Scanning electron microscope (SEM) images of (a) nanoparticles reproduced with permission.[103] Copyright 2013, Elsevier. (b) Nanorods reproduced with permission.[71] Copyright 2014, Royal Society of Chemistry. (c) Nanotubes reproduced with permission.[121] Copyright 2023, Royal Society of Chemistry. (d) Nanowires reproduced with permission.[58] Copyright 2015, Elsevier. Transmission electron microscope (TEM) images of (e) nanosheets reproduced with permission.[82] Copyright 2016, Elsevier. (f) Nano-octahedrons reproduced with permission.[59] Copyright 2023, Springer Nature.

nanospheres,[64,83,88] nanorods,[60,74,75,85,108] nanocuboids,[87] nanotubes,[122] nanosheets,[72,84] nano-octahedrons,[62,68] nanowires,[61,69,82] microplates,[77] microspheres[59,63,70,103,104] and hollow spheres.[71,73,79] Some examples are shown in Fig. 4. These structures provide a large surface area[62] for the electrolyte to interact with, shortening the Li^+ ion diffusion path and improving reaction kinetics.[124] Some structures are also porous and therefore have vacant space which can accommodate structural strain during cycling.[45] This leads to improved anode stability and cycling performance.[45,120]

Table 3 summarises the current literature on the electrochemical properties of pure Mn_3O_4 micro- and nano-sized

active materials for conversion-type anodes, in chronological order. Although initial discharge capacities often promise greater than 1000 mAh g^{-1}, there is always an initial capacity loss due to SEI layer formation, resulting in low coulombic efficiency for the first cycle.[120] These anodes also suffer from low capacity retention. The reversible capacity does not often meet the theoretical capacity of Mn_3O_4 (937 mAh g^{-1}). Le *et al.*[125] attributed this to volumetric expansion and the agglomeration of nanoparticles during cycling. Possible mitigation strategies include introducing stable surface coatings or artificial SEI layers, but further work is needed in this area.[45,57] In summary, designing micro- and nano- structures, have significantly increased the specific capacity to values much higher than that of graphite anodes (372 mAh g^{-1}).[74] However, more work is required to reduce expansion and particle agglomeration.

2.5 Mn_3O_4 hybrid LIB anodes

A recent approach is to design ternary hybrid anodes consisting of three materials.[120,126,127] For example, in 2024, Li *et al.*[120] designed a ternary Mn_2O_3/Mn_3O_4/C anode for LIBs which had a specific capacity of 608.5 mAh g^{-1} at 0.5 A g^{-1}. Its double-shelled structure is shown schematically in Fig. 5. However, these ternary hybrid anodes are costly, difficult to design and can still suffer from volume expansion.

An alternative approach is to combine Mn_3O_4 with carbon matrix materials (Fig. 6) such as graphene,[85,108] reduced graphene oxide (rGO),[50,67,78,86,107,109,110] carbon quantum dots,[128] carbon nanosheets[42] and carbon nanotubes.[124,129] These conductive carbon nanostructures can have high porosity[130] and high surface areas, providing more active sites for charge transfer and shortening the path length for electronic and ionic transport.[10,52] This results in a reduction in charge transfer resistance and improved conductivity of the anode.[131] Carbon matrix materials can also have high mechanical strength[130] and provide stable support during cycling,[110] resulting in a reduction in volume changes.[131] Further, the addition of carbon can mitigate particle agglomeration, increasing anode stability during cycling.[120]

Mn_3O_4 hybrid anodes are often Mn_3O_4 nanoparticles, nanorods or nanospheres which have been combined with graphene nanosheets, carbon nanosheets, exfoliated graphite or rGO (to be discussed in more detail in the following section) to provide a conductive, stable matrix. Mn_3O_4 has also been combined with various materials, such as nitrogen-doped (N-doped) carbon,[65] zinc oxide (ZnO),[79] hydrogenated titanium dioxide (TiO_2),[75] manganese carbonate ($MnCO_3$)[83] and Fe_2O_3.[132] These hybrid anodes offer high initial discharge capacities (615–2457 mAh g^{-1}) compared to pure Mn_3O_4 anodes. Reversible capacities are higher than that of graphite

Table 3 Electrochemical properties of micro- and nano-structured Mn_3O_4 anodes in half-cells

Morphology of Mn_3O_4 anode and diameter	Initial discharge capacity (mAh g^{-1})	Reversible capacity (mAh g^{-1})	Current density (mA g^{-1})	Capacity retention	C.E. (cycle)	Year	Ref.
Nanoparticles, 10–20 nm	—	115 (10 cycles)	40	—	—	2010	50
Nanoparticles, 14 nm	~530	150 (10 cycles)	60	—	<90% (3rd)	2013	105
Nanoparticles, 30 nm	1324.4	586.9 (30 cycles)	30.4	91.8%	—	2014	102
Porous nanorods, 120 nm	1453	901.5 (150 cycles)	500	99.3%	64.6% (1st)	2014	74
Nanowires, 100 nm	1844.3	400 (100 cycles)	200	—	60% (1st)	2015	61
Nanorods, 120 nm	1392	165 (100 cycles)	500	—	—	2015	75
Nanoparticles, 300–400 nm	918.3	400 (50 cycles)	100	—	58.5% (1st)	2015	76
Nanosheets, 4 nm	1149.9	520 (300 cycles)	200	—	—	2016	84
Hollow microspheres, 0.5 μm	1577.8	646.9 (240 cycles)	200	—	>95% (3rd)	2017	73
Microplates, 4.9 μm	~1500	665 (150 cycles)	300	—	98% (3rd)	2017	77
Nanorods, 200 nm	—	375 (100 cycles)	100	—	34% (1st)	2017	85
Nanospheres, <50 nm	1179	553 (100 cycles)	100	73%	—	2018	64
Nanoparticles, 200–400 nm	—	100 (60 cycles)	100	—	—	2018	106
Nanoparticles, 10–20 nm	1158	71 (100 cycles)	100	—	31.5% (1st)	2018	65
Nano-octahedrons, 100–150 nm	—	303 (200 cycles)	100	—	—	2019	78
Nanowires, 50–250 nm	1626	484 (100 cycles)	100	61%	—	2019	69
2D nanosheets, ~4 μm	1234	344 (50 cycles)	100	—		2019	72
Nano octahedrons, 400 nm	971.8	450 (300 cycles)	1000	76.6%	92.7% (3rd)	2020	68
Nanoparticles, 40 nm	1021	1345 (190 cycles)	200	—	65% (1st)	2022	68
Nanoparticles, 100–200 nm	1240	414 (100 cycles)	200	—	—	2022	107
Porous nanotubes, 530 nm	~1200	901.4 (100 cycles)	50	—	98% (3rd)	2023	122

C.E. = coulombic efficiency.

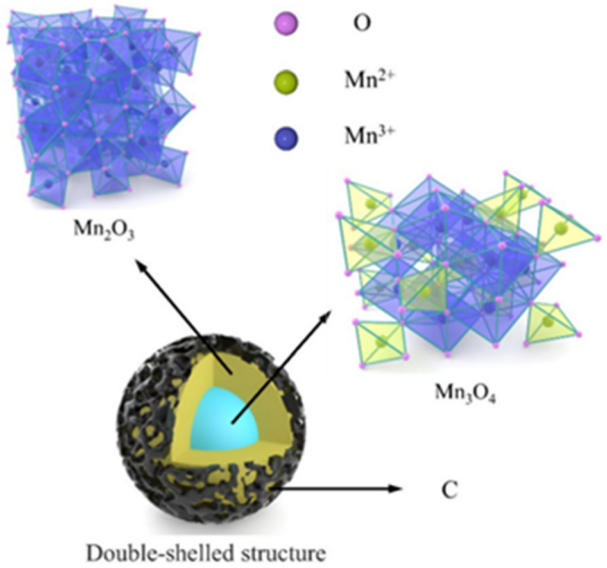

Fig. 5 A ternary anode of C, Mn_2O_3 and Mn_3O_4. Reproduced with permission.[119] Copyright 2024, Springer Nature.

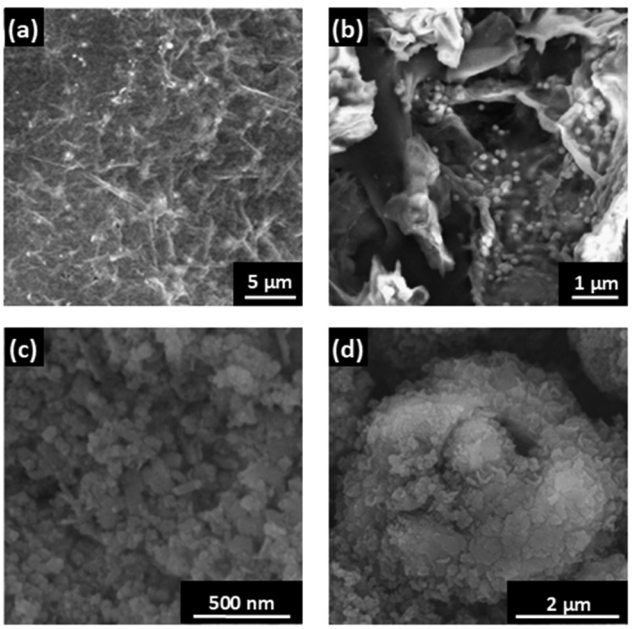

Fig. 6 Morphologies of Mn_3O_4 hybrid anodes. SEM images of (a) porous Mn_3O_4 nanorods in rGO paper. Reproduced with permission.[102] Copyright 2016, Elsevier. (b) rGO wrapped Mn_3O_4 nanoparticles. Reproduced with permission.[106] Copyright 2022, Elsevier. (c) Mn_3O_4 coated with carbon quantum dots. Reproduced with permission.[108] Copyright 2015, Royal Society of Chemistry. (d) Yolk–shell structured carbon/Mn_3O_4 microspheres. Reproduced with permission.[127] Copyright 2020, John Wiley and Sons.

(393–1522.8 mAh g^{-1}), however, capacity retention is not always reported, and the initial coulombic efficiency (ICE) remains low.

Table 4 summarises the current literature on Mn_3O_4 hybrid anodes in chronological order. Mn_3O_4/rGO anodes will be discussed separately in the next section.

2.6 Manganese oxide/rGO anodes

Mn_XO_Y/rGO anodes have gained attention in recent years due to their promising capacities and high stabilities.[60,86,108–110] rGO (Fig. 7, right) is a form of graphene (Fig. 7, left) with reduced oxygen content.[133] Graphene is a 2D structure consisting of a flat monolayer of carbon atoms arranged in a hexagonal, honeycomb lattice.[134]

rGO has desirable properties for energy storage, such as a high conductivity,[108] excellent mechanical strength[60] and high specific surface area for electrochemical reactions which can enhance ion diffusion in LIB anodes.[108] The nanostructure of rGO can also reduce electrochemical impedance,[108] provide stable support and act to prevent volume changes in Mn_XO_Y/rGO anodes during cycling.[135] The layered structure of rGO can also prevent aggregation of Mn_XO_Y nanoparticles.[110,136] The layers can behave as buffer layers, stopping pulverisation of nanoparticles during cycling.[108] Simultaneously, the Mn_XO_Y nanoparticles can prevent aggregation of graphene sheets which is a challenge in pure graphene and rGO anodes.[109] This synergistic effect between the two materials helps retain the mechanical stability and surface area of the Mn_XO_Y/rGO anode, enhancing electrochemical performance.[109]

There are multiple ways to produce Mn_XO_Y/rGO hybrids[108–110,136–141] (discussed below in section 2.6.1). To produce rGO (Fig. 7, right), however, graphene oxide (GO) must be used as a precursor (Fig. 7, middle).[142] GO is a heavily oxygenated single-layer of graphene (Fig. 7, left), containing epoxides, alcohol and carboxylic acid groups.[143] GO is a hydrophilic material due to the presence of polar oxygen functional groups, allowing it to be easily dispersed in water.[144] However, GO is not very useful in LIBs due to its low conductivity and excess of oxygen groups which can undergo parasitic electrochemical reactions.[145] rGO is typically obtained *via* chemical, thermal or electrochemical reduction of GO, the chemical composition of which depends on the reducing agent used. rGO (Fig. 7, right) has reduced oxygen content and while some oxygen functional groups remain, not all sp^3 bonds return to sp^2 bonds.[142] The presence of residual oxygen groups in rGO can be used as nucleation sites for nanoparticle growth and even help stabilise nanoparticles after growth, whilst retaining high conductivity.[146] This is indeed a unique advantage in using rGO rather than GO or pristine graphene in these hybrid anodes. The properties of GO and rGO are summarised in Table 5.

2.6.1 Methods to produce manganese oxide/rGO hybrids. Table 6 compares different manganese oxide/rGO hybrids and their manganese precursors for all synthesis methods. The common precursors are $KMnO_4$, manganese(II) acetate tetrahydrate ($Mn(Ac)_2{\cdot}4H_2O$) and various salts ($MnCl_2{\cdot}4H_2O$, $Mn(NO_3)_2{\cdot}4H_2O$ and $MnSO_4{\cdot}H_2O$).

Various methods have been used to synthesise manganese oxide/rGO hybrid materials. These include hydrothermal methods,[96,135–137,147–151] *in situ* exfoliation,[152] sol–gel methods,[49,153] solvothermal calcination,[154] microwave-assisted chemical precipitation,[169] reduction by Mn powder,[170] succes-

Table 4 Electrochemical properties of Mn_3O_4 hybrid anodes in half-cells

Anode	Morphology of hybrid anode and diameter	Initial discharge capacity (mAh g^{-1})	Reversible capacity (mAh g^{-1})	Current density (mA g^{-1})	Capacity retention	C.E. (cycle)	Year	Ref.
Mn_3O_4/graphene nanosheet	Nanoparticles, 10–20 nm	900	730 (40 cycles)	400	—	98% (4th)	2010	50
Mn_3O_4/graphene nanosheet	Nanoparticles, 14 nm	~730	500 (40 cycles)	60	—	>99% (4th)	2013	105
Mn_3O_4 carbon microspheres	Microspheres, ~1 μm	~1400	915 (50 cycles)	100	—	96% (3rd)	2015	103
Hydrogenated TiO_2—coated Mn_3O_4	Nanorods, 120 nm	~900	393 (100 cycles)	500	—	71.2% (1st)	2015	75
Mn_3O_4/Fe_3O_4	Nanoflowers, 150 nm	1625	600 (50 cycles)	100	—	68.4% (1st)	2015	76
Mesoporous Mn_3O_4/C	Microspheres, 5–25 μm	1500	1032 (200 cycles)	200	—	80.3% (1st)	2017	63
Mn_3O_4 on graphene nanosheet	Nanorods, 200 nm	1918.7	1155 (100 cycles)	100	—	56.5% (1st)	2017	85
Mn_3O_4 on exfoliated graphite	Nanoparticles, 7 nm	997	655 (120 cycles)	100	—	55.3% (1st)	2017	66
Mn_3O_4@C micro/nanocuboids	Nanocuboids, 0.5–1.5 μm	1460	879 (200 cycles)	100	86% (500 cycles)	58.4% (1st)	2018	87
Fluorinated Mn_3O_4	Nanospheres, <50 nm	1610	990 (100 cycles)	100	88%	86–90% (4th)	2018	64
Carbon-coated Mn_3O_4	Nanospheres, 400 nm	2022	1288 (190 cycles)	200	—	—	2018	88
Mn_3O_4 on graphene nanosheets	Nanoparticles, 200–400 nm	1450	930 (60 cycles)	100	—	—	2018	106
Mn_3O_4 on N-doped porous C microspheres	Nanoparticles, 10–20 nm	2163	1629 (100 cycles)	100	—	51.5% (1st)	2018	65
Carbon-coated Mn_3O_4 microspheres	Microspheres, 2 μm	1422.1	913.8 (300 cycles)	500	—	~100% (20th)	2019	70
Mn_3O_4/graphene	Nano octahedrons, 100–150 nm	—	474 (200 cycles)	100	—	—	2019	78
ZnO/$Mn3O_4$	Cage-like hollow nanospheres, 140–220 nm	1815	1091 (100 cycles)	200	—	—	2020	79
N-doped carbon Mn_3O_4 microspheres	Yolk shell layered microspheres, 0.6 μm	1294.7	1016 (250 cycles)	200	—	64.8% (1st)	2020	104
Graphene-coated carbon-coated $Mn3O_4$	Mn_3O_4 encapsulated in hollow C spheres, ~200 nm	972	557	100	91% after 50 cycles	—	2021	71
Mn_3O_4 on carbon nanotubes	Nanoparticles, 18 nm	1554.2	895 (200 cycles)	500	79.8%	66.7% (1st)	2021	80
Mn_3O_4/graphene	Nanoparticles, 100–200 nm	1420	1380 (150 cycles)	200	—	98.5% (1st)	2022	107
Graphene-wrapped $MnCO_3$/Mn_3O_4	Nanoparticles, 50 nm	2457.4	1522.8 (200 cycles)	500	—	—	2022	67
Mn_3O_4 in N-doped graphene	Nano-octahedrons, 20 nm	1004.4	898 (100 cycles)	100	—	97.5% (100th)	2023	62
Mn_3O_4 on Fe_2O_3 micro discs	Nanowires on micro discs of 5–8 μm	1483.9	713 (100 cycles)	500	—	—	2023	82
Mn_3O_4/carbon nanosheet	Nanoparticles, >5 nm	~615	603 (700 cycles)	2 C	98%	—	2024	42
$MnCO_3$–Mn_3O_4	Nanospheres, 300 nm on 10 μm microspheres	1099.2	654.8 (100 cycles)	1000	—	—	2024	83

C.E. = coulombic efficiency.

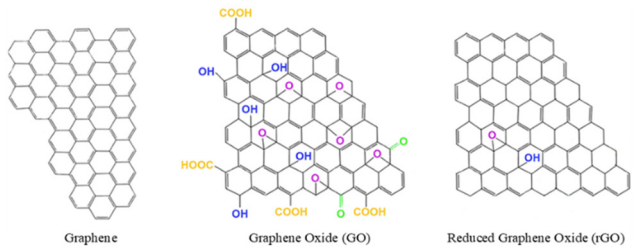

Fig. 7 Structures of graphene, GO and rGO. Reproduced with permission.[132] Copyright 2015, Royal Society of Chemistry.

Table 5 Properties of GO and rGO

Properties	GO	rGO	Ref.
Band gap (eV)	2.2	1–1.69	155
Electron mobility at room temperature ($cm^2 V^{-1} s^{-1}$)	0.1–10	2–200	156
Specific surface area ($m^2 g^{-1}$)	736.6	466–758	157–159
Electrical conductivity ($S m^{-1}$)	5.7×10^{-6}	10^2–10^5	158, 160–164
Sheet resistance (Ω sq^{-1})	~10^{10}–10^{12}	~10^2–10^6	156, 164, 165
Specific capacitance ($F g^{-1}$)	215–255	210–425	160, 166–168

sive ionic layer deposition,[171] ball-milling with chemical reduction[172] ultrasonication[48,99] and solution precipitation.[173] Table 7 compares different manganese oxide/rGO hybrids and their reagents and reaction conditions.

Overall the most common approach is hydrothermal synthesis.[135–137] involving a chemical reaction in aqueous solution in a sealed pressure vessel at high temperature.[147] Hydrothermal synthesis allows simultaneous reduction of GO to rGO as the crystallisation of nanoparticle Mn_3O_4 occurs.[109] It has also been shown to prevent rGO nanosheets from restacking, providing a higher surface area for electrochemical reactions.[109,171] Further, hydrothermal synthesis is a flexible method in which the temperature, reagents and reaction time can easily be controlled.

2.6.2 Electrochemical properties of manganese oxide/rGO hybrids. This section describes the electrochemical properties of manganese oxide/rGO hybrid anodes. As explained earlier, the research direction has shifted from MnO_2 to Mn_3O_4 hybrid anodes, as MnO_2 has proven to be more useful as a cathode material in zinc ion batteries.[174] In recent years, Mn_3O_4/rGO anode research has expanded due to their high capacities and promising capacity retentions.[60,86,108–110] Therefore, this material will be the focus of the remainder of this review. Table 8 summarises the current electrochemical literature on Mn_3O_4/rGO anodes in chronological order. Overall, adding rGO has been shown to increase the capacity of Mn_3O_4 and give a higher coulombic efficiency than that of pure Mn_3O_4 (often greater than 98% from the third cycle onwards).[60,86,108–110] For example, Chen *et al.*[110] wrapped Mn_3O_4 nanoparticles with rGO and compared the reversible capacity with bare Mn_3O_4 nanoparticles at 100 mAg^{-1} after 200 cycles. The rGO-wrapped Mn_3O_4 retained a reversible capacity of 795.5 mAh g^{-1}, whereas the bare Mn_3O_4 nanoparticles which only retained 193.4 mAh g^{-1}.[110] Electrochemical studies and ion diffusion rates of these anodes are discussed in the next section.

3. Electrochemical studies of Mn_3O_4/rGO hybrid anodes

3.1 Conversion mechanisms of Mn_3O_4/rGO anodes

The current understanding of Mn_3O_4 and Mn_3O_4/rGO anodes for LIBs is that they do not undergo a Li^+ ion intercalation mechanism like graphite.[180] Instead, they undergo a conversion mechanism involving a multi-electron transfer mechanism.[181]

To show this, Wang *et al.*[50] synthesised a Mn_3O_4/rGO anode and found that a reversible conversion reaction occurred during the first charge/discharge cycle, as shown in Fig. 8 and expressed as reaction (2)

Charging

$$Mn_3O_4 + 8\,Li^+ + 8\,e^- \leftrightarrow 3Mn^0 + 4\,Li_2O \quad (2)$$

Discharging

.

In Fig. 8, red (charge), Area 1 of the charge curve (1.2–0.4 V), indicates the formation of the SEI layer and decomposition of the solvent.[50] While Area 2, Fig. 8, red (with a voltage plateau at 0.4 V) represents the charging reaction in reaction (2), *i.e.* the formation of manganese metal, Mn^0, and lithium oxide, Li_2O during charging.[50] The plateau in the discharge curve at 1.2 V (Fig. 8, blue (discharge), Area 3) was attributed to the reverse reaction (2), and the re-formation of Mn_3O_4. After several cycles, the coulombic efficiency was greater than 98%, indicating good reversibility.[50]

Table 6 Manganese oxide/rGO hybrids from the literature and their precursors

	Precursor used					
Mn hybrid type	$KMnO_4$	$Mn(Ac)_2{\cdot}4H_2O$	$MnCl_2.4H_2O$	$Mn(NO_3)_2{\cdot}4H_2O$	$MnSO_4.H_2O$	Mn powder
MnO/rGO	Ref. 148					
MnO_2/rGO	Ref. 169, 175 and 176	Ref. 151			Ref. 169	Ref. 170
Mn_2O_3/rGO				Ref. 153		
Mn_3O_4/rGO	Ref. 48, 107, 110 and 136	Ref. 139 and 147	Ref. 49, 137, 154 and 177	Ref. 173	Ref. 48	
Mn_5O_8/rGO			Ref. 178			
MnO_x/rGO	Ref. 135, 150 and 179	Ref. 152			Ref. 152	

Table 7 Manganese oxide/rGO hybrids from the literature, their reagents and reaction conditions

Mn hybrid type	Reagents used	Reaction conditions	Ref
MnO/rGO	NH_4F	Heat in autoclave, 12 h, 160 °C	148
MnO_2/rGO	NH_4OH	Heat in autoclave, 24 h, 150 °C	151
	—	Microwave radiation, 300 °C	169
	Mn powder, HCl	—	170
	HCl	—	175
	$KMnO_4$, Na_2SO_4	—	176
Mn_2O_3/rGO	Ethylene glycol	Heat at 80 °C, heat in furnace, 4 h, 700 °C	153
Mn_3O_4/rGO	H_2SO_4	Heat at 50 °C for 5 h, heat, 10 h, 200 °C	110
	Ethylene glycol, CTAB, ethanolamine	Heat in autoclave, 12 h, 200 °C	137
	Polyethylene glycol	Heat in autoclave, 8 h, 130 °C	107
	Na_3Cit	Heat in autoclave, 10 h, 200 °C	147
	Na_2SO_3	2 h, 95 °C	136
	Urea, CTAB	Calcination, 700 °C	49
	Urea, ethylene glycol	Heat in autoclave, 24 h, 200 °C	154
	MnO_2	Heat in tube furnace, 2 h, 250 °C	48
	Hydrazine hydrate	Calcination, 4 h, 400 °C	173
	Absolute ethanol	Heat in autoclave, 24 h, 120 °C	139
	Ethanolamine	—	177
Mn_5O_8/rGO	NaOH	Calcination, 4 h, 400 °C	178
MnO_x/rGO	Treated carbon cloth	Heat in autoclave, 6 h, 150 °C, heat in autoclave, 2 h, 90 °C	135
	—	Ultrasonication method, heat in autoclave (conditions not provided)	150
	—	Electrochemical reduction	152
	HCl	Heat in autoclave, 8 h, 60 °C	179

Park *et al.*[108] synthesised porous Mn_3O_4 nanorods on rGO and used this directly as an LIB anode. They agreed that the mechanism followed reaction (2) and found good reversibility

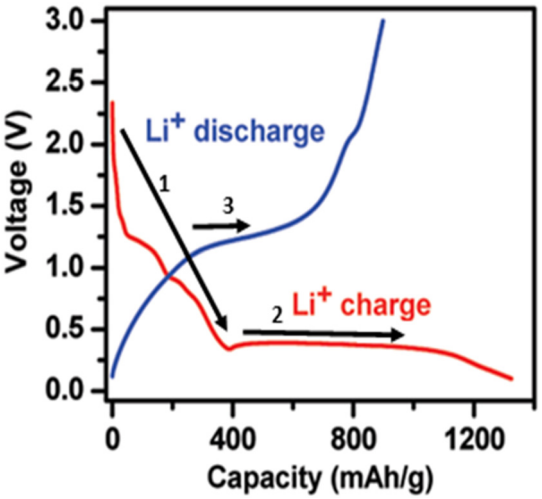

Fig. 8 Charge and discharge curve of the Mn_3O_4/rGO anode for the first cycle at a current density of 40 mA g^{-1} in a potential range of 0.1–3 V *vs.* Li^+/Li. Working electrode = Mn_3O_4/rGO : carbon black : PVDF in a mass ratio 80 : 10 : 10. Counter electrode = Li foil. Electrolyte = 1 M $LiPF_6$ in 1 : 1 EC and DEC. Reproduced with permission.[50] Copyright 2010, American Chemical Society.

in the second and fifth CV curve, as shown in Fig. 9a. Peaks were assigned as follows: Peak 1 at 0.13 V = reduction of Li^+ to Li_2O and Peak 2 at 1.3 V = oxidation of manganese metal to manganese ions.[108] Lv *et al.*[109] embedded Mn_3O_4 nanoparticles in rGO and used this directly as an anode without binder or conductive additive. They observed a peak in the anodic sweep at 1.15 V which was assigned to oxidation of manganese metal (Mn^0) to Mn^{2+}.[109] An additional peak at 1.97 V was assigned to oxidation of Mn^{2+} to Mn^{3+}, these are referred to in Fig. 9b as Peak 1 and Peak 2, respectively.[109]

Seong *et al.*[60] synthesised an acid-treated rGO/Mn_3O_4 nanorod composite and were also in agreement that the conversion reaction was reversible, however, they do suggest an intermediate stage in which manganese monoxide (MnO) is formed. Fig. 10 shows cyclic voltammograms and charge

Table 8 Electrochemical properties of Mn_3O_4/rGO anodes in half-cells

Morphology of Mn_3O_4/rGO anode and diameter	Initial discharge capacity (mAh g^{-1})	Reversible capacity (mAh g^{-1})	Current density (mA g^{-1})	Capacity Mn_3O_4 (mAh g^{-1})	Capacity retention	C.E. (cycle)	Year	Ref.
Mn_3O_4 nanorods, 60–120 nm on porous rGO	943	573 (100 cycles)	100	—	—	100% (3rd)	2016	108
Mn_3O_4 nanorods on acid-treated rGO	1130	749 (100 cycles)	200	—	—	98% (3rd)	2017	60
Mn_3O_4 nanoparticles, 45 nm in 3D rGO	681	696 (60 cycles)	200	86 at 100 mA g^{-1} after 15 cycles	~100%	98% (60th)	2017	109
Mn_3O_4 nanoparticles, 15–20 nm in rGO sheet	883.98	638 (150 cycles)	123	—	85%	96.1% (3rd)	2020	86
Mn_3O_4 nanoparticles, 50 nm wrapped with rGO	1359.6	795.5 (200 cycles)	100	193.4 at 100 mA g^{-1} after 200 cycles	87.4%	67% (1st)	2022	110

C.E. = coulombic efficiency.

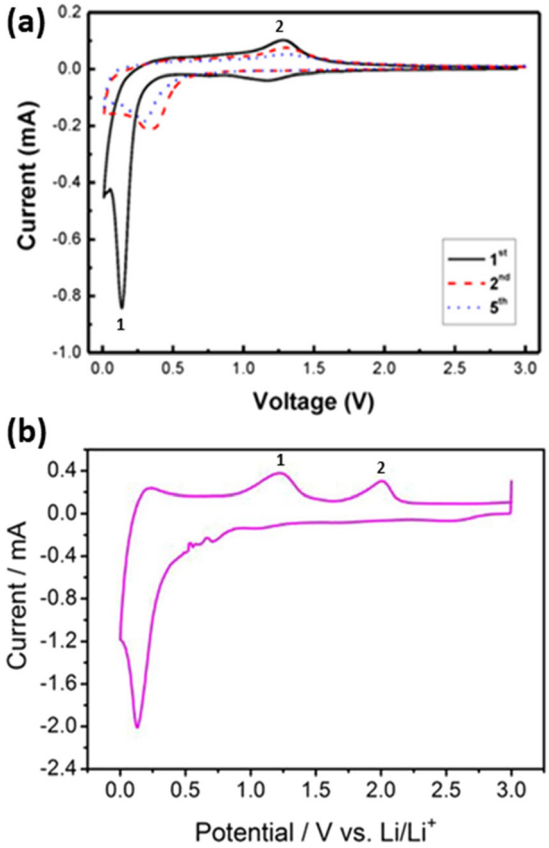

Fig. 9 Cyclic voltammograms of Mn_3O_4/rGO anodes at a scan rate of 0.1 mV s^{-1}. Working electrode = Mn_3O_4/rGO, no binder or conductive additive. Counter electrode = Li foil. (a) Potential range of 0.05–3 V in 1 M $LiPF_6$ in 1 : 1 EC and DEC. Reprinted with permission.[106] Copyright 2016, Elsevier. (b) Potential range of 0.01–3 V in 1 M $LiPF_6$ in 1 : 1 : 1 EC, DMC and DEC. Reproduced with permission.[107] Copyright 2017, Elsevier.

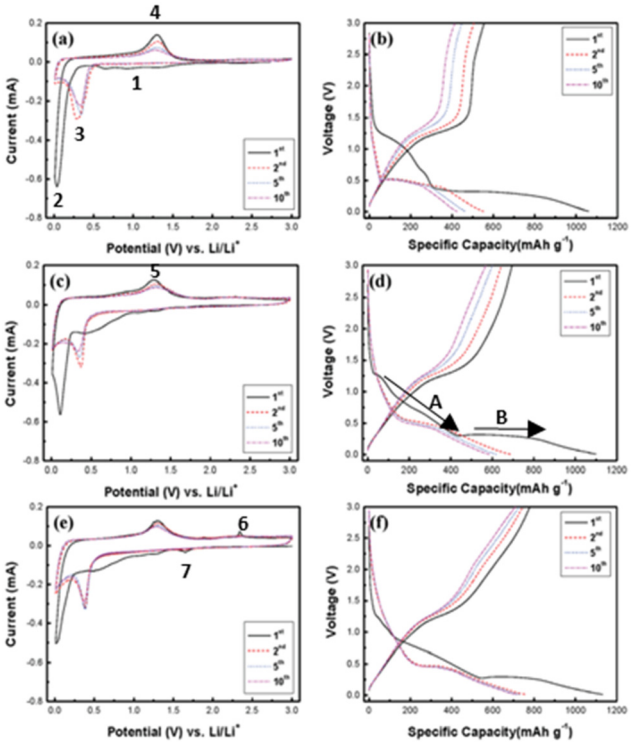

Fig. 10 Cyclic voltammograms and charge discharge curves of (a and b) Mn_3O_4 (c and d) Mn_3O_4/rGO and (e and f) acid-treated Mn_3O_4/rGO. They were tested at a scan rate of 0.1 mV s^{-1} in a potential range of 0.01–3 V *vs.* Li^+/Li. Working electrode = Active material : Super P : PVDF in a mass ratio of 70 : 20 : 10 in NMP. Electrolyte = 1 M $LiPF_6$ in 1 : 1 EC and DMC. Reproduced with permission.[57] Copyright 2017, Royal Society of Chemistry.

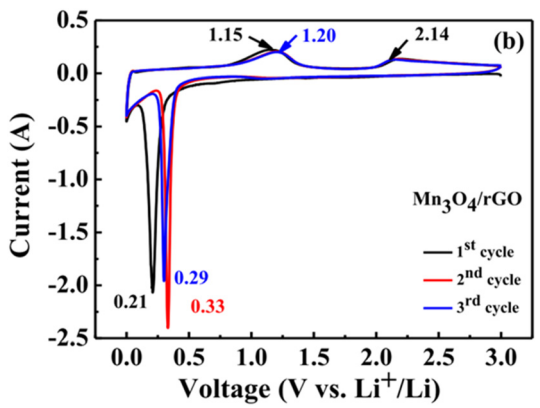

Fig. 11 Cyclic voltammograms of Mn_3O_4/rGO anode at a scan rate of 0.1 mV s^{-1} in a potential range of 0.01–3 V. Working electrode = Active material : Super P : LiOH:PAA in a mass ratio of 80 : 10 : 5 : 5. Counter electrode = Li foil. Electrolyte = 1 M $LiPF_6$ in 1 : 1 EC and DEC. Reproduced with permission.[84] Copyright 2020, Elsevier.

discharge curves of Mn_3O_4, Mn_3O_4/rGO and acid-treated Mn_3O_4/rGO. Peaks and areas are labelled as follows:[60]

- Plateau 1 at 0.5–1.9 V = formation of SEI layer and reduction of Mn_3O_4 in the first cycle;
- Peak 2 at 0.035 V = reduction of MnO to Mn^0 in the first cycle;
- Peak 3 at 0.35 V = shifting of peak 2 due to structural changes in first discharge cycle;
- Peak 4 at 1.3 V = oxidation of Mn^0 to MnO. Peak is stronger in Mn_3O_4/rGO (Peak 5 in Fig. 10c);
- Peak 6 at 2.34 V = oxidation of MnO to Mn_3O_4;
- Peak 7 at 1.65 V = reduction of Mn_3O_4 to MnO;
- Area A at 1.25–0.27 V = formation of SEI layer and reduction of Mn_3O_4 to MnO; and
- Area B at 0.27–0.01 V = reduction of MnO to Mn^0.

Weng *et al.*[86] synthesised a Mn_3O_4/rGO nanocomposite and gathered cyclic voltammetry data (Fig. 11 and Table 9). They also suggested an intermediate stage in which MnO was formed and assigned a peak at 1.15 V (Fig. 11) to oxidation of Mn^0 to MnO.[86] However, they also observed a peak at 2.14 V (Fig. 11) which was attributed to further oxidation of MnO to Mn_3O_4, indicating the reaction was reversible.[86]

Other researchers disagree that the conversion mechanism proposed for Mn_3O_4/rGO anodes (reaction (2)) is reversible

Table 9 Peak assignment for Fig. 11

Voltage (V)	Cycle	Peak assignment
0.21	1st	Reduction of Mn_3O_4 to Li_2O and Mn^0
0.29	3rd	
0.33	2nd	
1.15	1st	Oxidation of Mn^0 to MnO, decomposition of Li_2O
1.20	3rd	
2.14	1st	Further oxidation of MnO to Mn_3O_4

and that Mn_3O_4 is reformed. This is explained visually in Fig. 12.[180] In 2018, Su *et al.*[180] synthesised a nano-sized LIB using a Mn_3O_4/rGO anode inside a transmission electron microscope. In the first charge cycle, they found that Mn_3O_4 nanoparticles lithiate into manganese metal (Mn^0) nanograins embedded into a Li_2O matrix. However, this Mn^0 and Li_2O cannot be recovered to reform Mn_3O_4 (reaction (3)). After the first charge cycle, a reversible reaction occurs (reaction (4)) where Mn^0 is converted to MnO during charging and *vice versa* during discharging

$$\underset{\text{(First cycle)}}{\overset{\text{Charging}}{Mn_3O_4 + 8\,Li^+ + 8\,e^- \rightarrow 3\,Mn^0 + 4\,Li_2O}} \quad (3)$$

$$\underset{\text{(First delithiation onwards)}}{\overset{\text{Charging}}{\underset{\text{Discharging}}{Mn^0 + Li_2O \leftrightarrow MnO + 2\,Li^+ + 2\,e^-}}} \quad (4)$$

.[180]

In 2022, Chen *et al.*[110] synthesised rGO wrapped nanocomposites as LIB anode materials. The work supported that of Su *et al.*[180] that Mn_3O_4 is not reformed and that the reaction follows reactions (3) and (4). In cyclic voltammetry measurements, they observed an oxidation peak at 0.8 V which was assigned to oxidation of Mn^0 to manganese ions and decomposition of Li_2O.[110] In the galvanostatic discharge charge curve, they observed a plateau at 0.25 V in the first cycle which was assigned to the reduction of Mn^{2+} and Mn^{3+} in Mn_3O_4/rGO to Mn^0. The group attributed the voltage plateaus at 0.5 V in the following cycles to conversion between Mn^0 and MnO described in reaction (4).[110]

Clearly, there are some discrepancies in the literature, so further work is needed to better understand and fully confirm the conversion mechanism for Mn_3O_4/rGO anodes. Fig. 13 summarises what is known so far about the conversion mechanism in Mn_3O_4/rGO anodes and relates this to changes in potential.

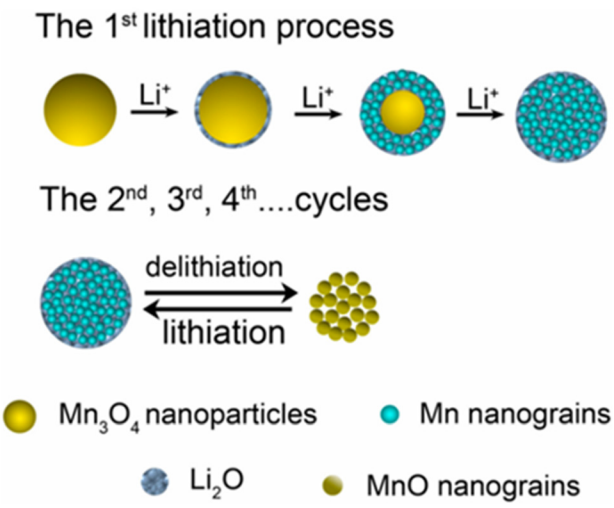

Fig. 12 A schematic showing the conversion mechanism of Mn_3O_4 (graphene is not shown). Working electrode = Mn_3O_4/rGO on Au wire. Counter electrode = Li metal attached to tungsten wire. Electrolyte = solid naturally grown Li_2O layer. Reproduced with permission.[178] Copyright 2018, American Chemical Society.

3.2 Charge transfer resistance and ion diffusion in Mn_3O_4/rGO anodes

A small number of groups[78,86,110] have measured electrochemical impedance spectroscopy (EIS) spectra for GO, rGO, MnO_2, MnO_2/rGO, Mn_3O_4, and Mn_3O_4/rGO. Table 10 summarises the charge-transfer resistance (R_{CT}) values, determined

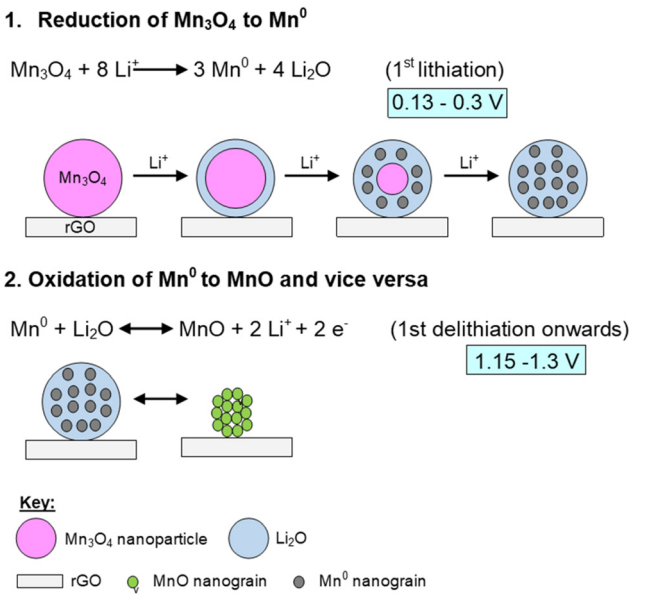

Fig. 13 A schematic showing a proposed conversion mechanism in Mn_3O_4/rGO anodes, along with potential ranges.

Table 10 Charge-transfer resistance values (R_{CT}) values.[78,86,110]

Material	R_{CT} (Ω)	D_{Li^+} ($cm^2\ s^{-1}$)
GO	156.3[86]	7.32×10^{-12}
rGO	68[86], 43.4[110]	1.85×10^{-10}
MnO_2	68.1[86]	1.3×10^{-10}
MnO_2/rGO	76.2[86]	4.7×10^{-11}
Mn_3O_4	102.3,[110] 108[78]	—

from the diameter of the semi-circles in Nyquist plots. Compared to all the materials tested (Table 10), the Mn_3O_4/rGO anode showed the lowest R_{CT} values, which could be attributed to fast charge-transport kinetics.[86]

To further understand the ion diffusion rates, Weng *et al.*[86] have been the only workers so far to have reported Li^+ ion diffusion coefficients (D_{Li^+}) for Mn_3O_4/rGO anodes using EIS. They found that the D_{Li^+} was fastest for Mn_3O_4/rGO anodes at 2.4×10^{-10} cm^2 s^{-1} compared to GO (7.32×10^{-12} cm^2 s^{-1}), rGO (1.85×10^{-10} cm^2 s^{-1}), MnO_2 (1.3×10^{-10} cm^2 s^{-1}) and MnO_2/rGO (4.7×10^{-11} cm^2 s^{-1}). Again, inferring superior charge-transfer kinetics in Mn_3O_4/rGO anodes.[86] Further studies are needed in this area.

4. Conclusions and future outlook

In summary, graphite is used in intercalation-type anodes, which are commonly used in LIBs. However, graphite is hindered by various factors including slow kinetics,[11] a limited specific capacity[13,14] of 372 mAh g^{-1}, instability and thickening of the SEI layer,[12] volume changes (around 9%) during cycling[12] and lithium plating and dendrite formation during fast charging, as well as environmental concerns.[11] Therefore, alternative anode materials must be investigated which offer high capacities, high energy density and long cycle life, whilst also being inexpensive and environmentally friendly.

Mn_3O_4 and Mn_3O_4 hybrids have shown great promise as active materials for conversion-type LIB anodes in half-cell set-ups. Herein, coin cell components and potential ranges of promising manganese oxide and manganese oxide hybrid anodes in the literature were reviewed and compared, along with their morphologies and subsequent electrochemical properties such as initial discharge capacity, capacity retention and coulombic efficiency.

Manganese oxides are environmentally friendly, inexpensive,[45] highly abundant, provide excellent safety for LIBs and offer higher specific capacities than graphite (756–1223 mAh g^{-1}).[41] However, they are plagued by low conductivity, poor coulombic efficiencies and volume changes during cycling.[45]

Two approaches have been utilised to relieve these issues. The first is the design of manganese oxide nano- and microstructures to increase the surface area and improve reaction kinetics.[62] The most common synthesis method to make these materials is a hydrothermal route. This approach has increased the specific capacity to values much higher than that of graphite anodes, however the theoretical capacities are not reached. Further work is required here to reduce volume expansion and particle agglomeration.

The second approach is to combine manganese oxides with conductive carbon materials, for example, through carbon coating or hybridisation with rGO. These structures can have high surface area and porosity, providing more active sites for charge transfer, shortening the path length for electronic and ionic transport and improving conductivity.[10,52] They also have high mechanical strength[130] and provide stable support during cycling,[110] resulting in a reduction in volume changes.[131]

Mn_XO_Y/rGO anodes have gained attention in recent years due to their promising capacities (up to 1360 mAh g^{-1} for Mn_3O_4/rGO)[110] and high capacity retention.[60,86,108–110] rGO has desirable properties for LIB anodes including high conductivity,[108] excellent mechanical strength[60] and high specific surface area, enhancing ion diffusion and providing structural support.[108] The unique layered structure of rGO can also prevent aggregation of Mn_3O_4 nanoparticles.[110,136]

Although there are excellent initial discharge specific capacities reported for these materials, further work is needed as follows:

(1) **Cycling stability and mass loading.** Despite the stringent reporting requirements for publication in the LIB community,[182–184] there remain very few studies on the long-term stability of these anodes (>300 cycles) or their performance at high current densities. Future LIB anode materials must retain their capacity at these high current densities for EVs which require fast charging. Moreover, the mass loading of active material is often unreported in literature. A study of how this affects the electrochemical performance would be very insightful. To improve benchmarking, future studies should report the initial coulombic efficiency (ICE) at a specific mass loading *e.g.* 1.0 mg cm^{-2}.

(2) **Voltage hysteresis, volume changes and SEI formation.** The voltage hysteresis (ΔV), volume changes during cycling and the stability of the SEI layer are seldom reported. These should be studied by using *in situ* transmission electron microscopy (TEM), scanning electron microscopy (SEM) and energy-dispersive X-ray (EDX) spectroscopy to compare anodes before and after cycling. The SEI layer is known to be anode dependent, and its composition on manganese oxide surfaces remains largely unexplored. First-cycle irreversible capacity loss due to Li^+ ion consumption to form the SEI layer is an inherent feature of LIBs. Although materials such as rGO improve capacity retention and structural stability, they cannot fully prevent lithium loss associated with SEI development. Future studies should therefore focus on mitigation strategies, such as artificial SEI layers and electrolyte additives, as well as reporting the first-cycle initial coulombic efficiency (ICE).

(3) **Reaction mechanisms.** While known that Mn_3O_4/rGO undergoes a conversion mechanism, there are discrepancies in the literature and the correct mechanism has not yet been agreed on. Techniques such as XRD (X-ray diffraction) should be employed to confirm the reaction pathway.

(4) **Charge-transfer and ion diffusion.** The literature is often lacking critical electrochemical impedance (EIS) studies, which can offer important information such as charge-transfer resistance and ion diffusion rates. Ion diffusion rates of Mn_XO_Y anodes are not well understood, and further investigation is needed here along with ion diffusion coefficient calculations.

(5) **Structure–property relationships.** Current research lacks an investigation into true structure–property relationships for

Mn_XO_Y and Mn_XO_Y hybrid anodes. For instance, it remains unclear how particle size and shape truly affect the specific capacity and ion diffusion rates. Future studies should also quantify the porosity of these anodes and the effect of pore size on Li^+ ion diffusion, capacity retention and CE. Control over morphology, size, porosity and uniformity of active material are vital to obtain high performance Mn_XO_Y anodes. For example, many different Mn_XO_Y nano- and microstructures have been developed, but the tailoring of Mn_XO_Y particle size to improve the efficacy of LIB anodes has not yet been explored in detail. Controlling the Mn_XO_Y particle size could be one way to improve reaction kinetics of Mn_XO_Y anodes. For example, in 2024, Liang *et al.*[42] synthesised Mn_3O_4 nanoparticles in carbon microspheres for LIB anodes. They found that decreasing particle size can increase the surface area and improve ion diffusion.[42]

(6) **Sustainability and scalable processing.** While Mn_XO_Y anodes are promising, they are still being considered at the laboratory scale. In order to make an impact in the LIB industry, beyond an edge case or scientific curiosity, the energy balance and environmental impacts of their production must be considered and addressed. In particular, more environmentally friendly synthesis routes and binders need to be investigated. Current literature mainly uses PVDF binder in NMP solvent to make these anodes which is toxic and harmful to the environment.[185]

(7) **Full-cell validation under realistic conditions.** Although Mn_XO_Y anodes have shown promising behaviour in half-cells, their integration into practical full-cell configurations remains limited.[57–59] Future research should focus on pairing these anodes with commercial cathode materials to evaluate their electrochemical behaviour under realistic lithium-ion battery conditions.

Despite the challenges mentioned above, the research area of Mn_XO_Y anodes, especially Mn_3O_4, Mn_3O_4 hybrid and Mn_3O_4/rGO anodes has a bright future due to the development of nanotechnology and advancements in battery-testing and characterisation techniques.

Author contributions

Lucy McElhone: conceptualisation, writing – original draft, writing – review and editing, visualisation. Amanda V. Ellis: conceptualisation, writing – original – draft, writing – review and editing, supervision, funding acquisition. Peter C. Sherrell: writing – review and editing. Andrew Thomas: writing – review and editing. Aravind Vijayaraghavan: writing – review and editing, supervision, funding acquisition.

Conflicts of interest

The authors declare that they have no known competing financial interests or personal relationships that could have appeared to influence the work in this paper.

Data availability

Data is available on request from the corresponding author, upon reasonable request.

Acknowledgements

LM acknowledges funding from the Cookson Scholar's Program (Manchester Melbourne Dual Award PhD Scholarship between the University of Manchester and the University of Melbourne). LM also acknowledges her President's Doctoral Scholar (PDS) Award from the University of Manchester.

PCS acknowledges support from RMIT University through the RMIT Vice Chancellor's Fellowship Scheme (2023).

References

1 J. M. Tarascon and M. Armand, *Nature*, 2001, **414**, 359–367.
2 D. Lin, Y. Liu and Y. Cui, *Nat. Nanotechnol.*, 2017, **12**, 194–206.
3 M. S. Whittingham, *Science*, 1976, **192**, 1126–1127.
4 J. B. Goodenough and K. S. Park, *J. Am. Chem. Soc.*, 2013, **135**, 1167–1176.
5 A. Yoshino, *Angew. Chem., Int. Ed.*, 2012, **51**, 5798–5800.
6 S. Basu, C. Zeller, P. J. Flanders, C. D. Fuerst, W. D. Johnson and J. E. Fischer, *Mater. Sci. Eng.*, 1979, **38**, 275–283.
7 N. A. Godshall, I. D. Raistrick and R. A. Huggins, *Mater. Res. Bull.*, 1980, **15**, 561–570.
8 K. Mizushima, P. C. Jones, P. J. Wiseman and J. B. Goodenough, *Mater. Res. Bull.*, 1980, **15**, 783–789.
9 M. Armand and J. M. Tarascon, *Nature*, 2008, **451**, 652–657.
10 L. Li, D. Zhang, J. Deng, Y. Gou, J. Fang, H. Cui, Y. Zhao and M. Cao, *Carbon*, 2021, **183**, 721–734.
11 C. Zhong, S. Weng, Z. Wang, C. Zhan and X. Wang, *Nano Energy*, 2023, **117**, 108894.
12 S. Chen, C. Liu, R. Feng, Z. Chen, Y. Lu, L. Chen, Q. Huang, Y. Guan, W. Yan, Y. Su, N. Li and F. Wu, *Chem. Eng. J.*, 2025, **503**, 158116.
13 R. Raccichini, A. Varzi, S. Passerini and B. Scrosati, *Nat. Mater.*, 2015, **14**, 271–279.
14 N. Nitta, F. Wu, J. T. Lee and G. Yushin, *Mater. Today*, 2015, **18**, 252–264.
15 J. T. Warner, in *Lithium-Ion Battery Chemistries*, ed. J. T. Warner, Elsevier, Amsterdam, 2019, ch. 3, pp. 43–77.
16 X. Yi, G. Qi, X. Liu, C. Depcik and L. Liu, *J. Energy Storage*, 2024, **95**, 112480.
17 P. G. Bruce, B. Scrosati and J.-M. Tarascon, *Angew. Chem., Int. Ed.*, 2008, **47**, 2930–2946.
18 X. Han, L. Lu, Y. Zheng, X. Feng, Z. Li, J. Li and M. Ouyang, *eTransportation*, 2019, **1**, 100005.

19 S. J. An, J. Li, C. Daniel, D. Mohanty, S. Nagpure and D. L. Wood, *Carbon*, 2016, **105**, 52–76.
20 S. Bhattacharya, A. R. Riahi and A. T. Alpas, *Carbon*, 2014, **77**, 99–112.
21 J. H. Park, H. Yoon, Y. Cho and C.-Y. Yoo, *Materials*, 2021, **14**, 4683.
22 K. Persson, V. A. Sethuraman, L. J. Hardwick, Y. Hinuma, Y. S. Meng, A. van der Ven, V. Srinivasan, R. Kostecki and G. Ceder, *J. Phys. Chem. Lett.*, 2010, **1**, 1176–1180.
23 J. Kim, S. M. Nithya Jeghan and G. Lee, *Microporous Mesoporous Mater.*, 2020, **305**, 110325.
24 S. Liu, B. Gu, Z. Chen, R. Zhan, X. Wang, R. Feng and Y. Sun, *J. Energy Chem.*, 2024, **91**, 484–500.
25 C. Sun, X. Ji, S. Weng, R. Li, X. Huang, C. Zhu, X. Xiao, T. Deng, L. Fan, L. Chen, X. Wang, C. Wang and X. Fan, *Adv. Mater.*, 2022, **34**, 2206020.
26 N. R. Chowdhury, A. J. Smith, K. Frenander, A. Mikheenkova, R. W. Lindström and T. Thiringer, *J. Energy Storage*, 2024, **76**, 110001.
27 L. Weber, *Mineral. Petrol.*, 2023, **117**, 387–399.
28 S. Zhao, S. Cheng, B. Xing, M. Ma, C. Shi, G. Cheng, W. Meng and C. Zhang, *J. Mater. Res. Technol.*, 2022, **21**, 4212–4223.
29 Q. Q. Zhang, X. Z. Gong and X. C. Meng, *Mater. Sci. Forum*, 2018, **913**, 1011–1017.
30 W. Cai, Y.-X. Yao, G.-L. Zhu, C. Yan, L.-L. Jiang, C. He, J.-Q. Huang and Q. Zhang, *Chem. Soc. Rev.*, 2020, **49**, 3806–3833.
31 A. Tomaszewska, Z. Chu, X. Feng, S. O'Kane, X. Liu, J. Chen, C. Ji, E. Endler, R. Li, L. Liu, Y. Li, S. Zheng, S. Vetterlein, M. Gao, J. Du, M. Parkes, M. Ouyang, M. Marinescu, G. Offer and B. Wu, *eTransportation*, 2019, **1**, 100011.
32 J. T. Warner, in *Lithium-Ion Battery Chemistries*, ed. J. T. Warner, Elsevier, Amsterdam, 2019, ch. 6, pp. 115–138.
33 J. She, H. Jin and H. Ji, *ChemElectroChem*, 2024, **11**, e202300706.
34 S.-H. Yu, X. Feng, N. Zhang, J. Seok and H. D. Abruña, *Acc. Chem. Res.*, 2018, **51**, 273–281.
35 H. Xu, H. Li and X. Wang, *ChemElectroChem*, 2023, **10**, e202201151.
36 S. Fang, D. Bresser and S. Passerini, *Adv. Energy Mater.*, 2020, **10**, 1902485.
37 K. Wang, Y. Wang, Y. Zhang, F. Liu, J. Shi, S. Liu, X. Xie, G. Cao and A. Pan, *Nanoscale*, 2020, **12**, 12623–12631.
38 M. S. Chandrasekar and S. Mitra, *Electrochim. Acta*, 2013, **92**, 47–54.
39 J. Jiang, S. Hu, X. Zhang, S. Li, H. Wei, B. Ren, S. Li, G. Chen, J. Yang, C. Han and Z. Liu, *Adv. Mater.*, 2024, **36**, 2311926.
40 P. Poizot, S. Laruelle, S. Grugeon, L. Dupont and J. M. Tarascon, *Nature*, 2000, **407**, 496–499.
41 S. H. Yu, S. H. Lee, D. J. Lee, Y. E. Sung and T. Hyeon, *Small*, 2016, **12**, 2146–2172.
42 H. Liang, Y. Liu, M. Song, X. Wang, Y. Song and X. Huang, *J. Alloys Compd.*, 2024, **976**, 173037.
43 Q. L. Reyes-Morales, J. R. Rangel-Mendez and L. F. Chazaro-Ruiz, *Sustainable Energy Fuels*, 2025, **9**, 1020–1028.
44 E. Zhu, Y. Geng, S. Xiao, T. Guo, Z. Gao and Z. Gao, *Resour. Environ. Sustain.*, 2024, **16**, 100152.
45 Y. Deng, L. Wan, Y. Xie, X. Qin and G. Chen, *RSC Adv.*, 2014, **4**, 23914–23935.
46 P. De, L. Bharti, J. Halder, S. Priya and A. Chandra, *Electrochim. Acta*, 2023, **469**, 143248.
47 J. Cabana, L. Monconduit, D. Larcher and M. R. Palacín, *Adv. Mater.*, 2010, **22**, E170–E192.
48 Z. Huang, S. Li, Z. Li, J. Li, G. Zhang, L. Cao and H. Liu, *J. Alloys Compd.*, 2020, **830**, 154637.
49 A. Gangwar, T. Das, S. K. Shaw and N. K. Prasad, *Electrochim. Acta*, 2021, **390**, 138823.
50 H. Wang, L.-F. Cui, Y. Yang, H. Sanchez Casalongue, J. T. Robinson, Y. Liang, Y. Cui and H. Dai, *J. Am. Chem. Soc.*, 2010, **132**, 13978–13980.
51 J. H. Albering, in *Handbook of Battery Materials*, ed. C. Daniel and J. O. Besenhard, Wiley-VCH, Weinheim, 2nd edn, 2011, ch. 3, pp. 87–123.
52 W. Wei, X. Cui, W. Chen and D. G. Ivey, *Chem. Soc. Rev.*, 2011, **40**, 1697–1721.
53 S. K. Ghosh, *ACS Omega*, 2020, **5**, 25493–25504.
54 R. D. W. Kemmitt, in *The Chemistry of Manganese, Technetium and Rhenium*, ed. R. D. W. Kemmitt and R. D. Peacock, Pergamon Press, Oxford, 1973, vol. 3, ch. 1, pp. 771–876.
55 Y. Zhong, X. Xia, J. Zhan, X. Wang and J. Tu, *J. Mater. Chem. A*, 2016, **4**, 11207–11213.
56 W. K. Mahmood and A. N. Naje, *Chem. Methodol.*, 2022, **6**, 985–996.
57 J. Zhang, R. Chu, Y. Chen, Y. Zeng, Y. Zhang and H. Guo, *Electrochim. Acta*, 2019, **319**, 518–526.
58 M. Li, B. Yu, W. Ma, X. Fei, G. Cheng, H. Gao and Z. Zhang, *Electrochim. Acta*, 2024, **504**, 144947.
59 X. Gu, J. Yue, L. Li, H. Xue, J. Yang and X. Zhao, *Electrochim. Acta*, 2015, **184**, 250–256.
60 C. Y. Seong, S. K. Park, Y. Bae, S. Yoo and Y. Piao, *RSC Adv.*, 2017, **7**, 37502–37507.
61 D. W. Yu, Y. L. Hou, X. Han, X. J. Zheng, S. J. Yu, Y. M. Chen and X. L. Wang, *Mater. Lett.*, 2015, **159**, 182–184.
62 P. Nagaraja, H. S. Rao, V. Pamidi, E. Umeshbabu, G. R. Rao and P. Justin, *Ionics*, 2023, **29**, 2587–2598.
63 H. J. Peng, G. X. Hao, Z. H. Chu, J. Lin, X. M. Lin and Y. P. Cai, *Cryst. Growth Des.*, 2017, **17**, 5881–5886.
64 N. Palaniyandy, F. P. Nkosi, K. Raju and K. I. Ozoemena, *Mater. Chem. Phys.*, 2018, **209**, 65–75.
65 L. Guo, Y. Ding, C. Qin, W. Song, S. Sun, K. Fang, W. Li, J. Du and F. Wang, *J. Alloys Compd.*, 2018, **735**, 209–217.
66 Y. Zhao, C. Ma and Y. Li, *Chem. Phys. Lett.*, 2017, **673**, 19–23.
67 J. Chen, X. Hu, H. Gao, S. Yan, S. Chen and X. Liu, *J. Mater. Sci. Technol.*, 2022, **99**, 9–17.
68 Y. Kong, R. Jiao, S. Zeng, C. Cui, H. Li, S. Xu and L. Wang, *Nanomaterials*, 2020, **10**, 367.

69 N. Palaniyandy, F. P. Nkosi, K. Raju and K. I. Ozoemena, *J. Electroanal. Chem.*, 2019, **833**, 79–92.
70 P. Chen, G. Zheng, S. Li, Z. Wang, G. Guo, J. Tang, Z. Wen, S. Ji, J. Cui and J. Sun, *Solid State Ionics*, 2019, **338**, 121–126.
71 E. Thauer, X. Shi, S. Zhang, X. Chen, L. Deeg, R. Klingeler, K. Wenelska and E. Mijowska, *Energy*, 2021, **217**, 119399.
72 N. Jarulertwathana, X. Jin and S. J. Hwang, *Emergent Mater.*, 2019, **2**, 487–494.
73 Z. Jiang, K. Huang, D. Yang, S. Wang, H. Zhong and C. Jiang, *RSC Adv.*, 2017, **7**, 8264–8271.
74 Z. Bai, X. Zhang, Y. Zhang, C. Guo and B. Tang, *J. Mater. Chem. A*, 2014, **2**, 16755–16760.
75 N. Wang, J. Yue, L. Chen, Y. Qian and J. Yang, *ACS. Appl. Mater. Interfaces*, 2015, **7**, 10348–10355.
76 D. Zhao, Q. Hao and C. Xu, *Electrochim. Acta*, 2015, **180**, 493–500.
77 F. X. Ma, H. B. Wu, X. Y. Sun, P. P. Wang, L. Zhen and C. Y. Xu, *ChemElectroChem*, 2017, **4**, 2703–2708.
78 S. P. Varghese, B. Babu, R. Prasannachandran, R. Antony and M. M. Shaijumon, *J. Alloys Compd.*, 2019, **780**, 588–596.
79 W. Zhanga, J. Chena, J. Nia, Y. Yanga, Y. Wanga, J. Chena, J. Lia, H. Yua, R. Guana and L. Yuea, *Mater. Lett.*, 2020, **260**, 126917.
80 K. Cao, Y. Jia, S. Wang, K. J. Huang and H. Liu, *J. Alloys Compd.*, 2021, **854**, 157179.
81 L. H. Wang, L. L. Ren, Y. F. Qin, J. Chen, H. Y. Chen, K. Wang, H. J. Liu, Z. Huang and Q. Li, *Int. J. Electrochem. Sci.*, 2022, **17**, 220221.
82 X. Zeng, Y. Ding, H. Bai, Q. Ding, X. Lin, J. Liu and Z. Sun, *Nanotechnology*, 2023, **34**, 325401.
83 G. Du, P. Gong, M. Hu, C. Cui, S. Zeng and L. Wang, *Int. J. Electrochem. Sci.*, 2024, **19**, 100771.
84 M. Zhen, Z. Zhang, Q. Ren and L. Liu, *Mater. Lett.*, 2016, **177**, 21–24.
85 L. L. Wu, D. L. Zhao, X. W. Cheng, Z. W. Ding, T. Hu and S. Meng, *J. Alloys Compd.*, 2017, **728**, 383–390.
86 S.-C. Weng, S. Brahma, P.-C. Huang, Y.-C. Huang, Y.-H. Lee, C.-C. Chang and J.-L. Huang, *Appl. Surf. Sci.*, 2020, **505**, 144629.
87 Y. Jiang, J. L. Yue, Q. Guo, Q. Xia, C. Zhou, T. Feng, J. Xu and H. Xia, *Small*, 2018, **14**, 1704296.
88 K. Liu, F. Zou, Y. Sun, Z. Yu, X. Liu, L. Zhou, Y. Xia, B. D. Vogt and Y. Zhu, *J. Power Sources*, 2018, **395**, 92–97.
89 O. Y. Gorbenko, I. E. Graboy, V. A. Amelichev, A. A. Bosak, A. R. Kaul, B. Güttler, V. L. Svetchnikov and H. W. Zandbergen, *Solid State Commun.*, 2002, **124**, 15–20.
90 D. Jia, K. Hanna, G. Mailhot and M. Brigante, *Molecules*, 2021, **26**, 5748.
91 S. V. Ovsyannikov, A. M. Abakumov, A. A. Tsirlin, W. Schnelle, R. Egoavil, J. Verbeeck, G. Van Tendeloo, K. V. Glazyrin, M. Hanfland and L. Dubrovinsky, *Angew. Chem., Int. Ed.*, 2013, **52**, 1494–1498.
92 M. M. Abdullah, S. A. Siddiqui and S. M. Al-Abbas, *J. Electron. Mater.*, 2020, **49**, 4410–4417.
93 S. V. Ovsyannikov, A. A. Tsirlin, I. V. Korobeynikov, N. V. Morozova, A. A. Aslandukova, G. Steinle-Neumann, S. Chariton, S. Khandarkhaeva, K. Glazyrin, F. Wilhelm, A. Rogalev and L. Dubrovinsky, *Inorg. Chem.*, 2021, **60**, 13348–13358.
94 M. Imperor-Clerc, D. Bazin, M.-D. Appay, P. Beaunier and A. Davidson, *Chem. Mater.*, 2004, **16**, 1813–1821.
95 X. Zhao, F. Zhang, H. Li, H. Dong, C. Yan, C. Meng, Y. Sang, H. Liu, Y. G. Guo and S. Wang, *Energy Environ. Sci.*, 2024, **17**, 3629–3640.
96 T. Niu, J. Li, Y. Qi, X. Huang and Y. Ren, *J. Mater. Sci.*, 2021, **56**, 16582–16590.
97 F. Zhang, N. Duan, J. Zuo, L. Jiang, J. Li, S. Zhuang, Y. Liu and F. Xu, *Chem. Eng. J.*, 2023, **476**, 146475.
98 X. Xu, Y. Zhou, Z. Feng, N. U. Kahn, Z. U. Haq Khan, Y. Tang, Y. Sun, P. Wan, Y. Chen and M. Fan, *ChemPlusChem*, 2018, **83**, 521–528.
99 P. Sen, S. Rana and A. De, *J. Electron. Mater.*, 2019, **49**, 763–772.
100 J. Zheng, R. Xia, S. Baiju, Z. Sun, P. Kaghazchi, J. E. ten Elshof, G. Koster and M. Huijben, *ACS Nano*, 2023, **17**, 25391–25404.
101 F. Fasulo, A. B. Muñoz-García, A. Massaro, O. Crescenzi, C. Huang and M. Pavone, *J. Mater. Chem. A*, 2023, **11**, 5660–5669.
102 H. Zhu, P. Ding, S. Fang and H. Liu, *Appl. Mech. Mater.*, 2014, **687–691**, 4331–4334.
103 S. Z. Huang, Y. Cai, J. Jin, J. Liu, Y. Li, Y. Yu, H. E. Wang, L. H. Chen and B. L. Su, *Nano Energy*, 2015, **12**, 833–844.
104 Y. Xu, Y. Qiu, C. Zhang, C. Gan, L. Huang, X. Tang and X. Luo, *Energy Technol.*, 2020, **8**, 2000376.
105 I. Nam, N. D. Kim, G. P. Kim, J. Park and J. Yi, *J. Power Sources*, 2013, **244**, 56–62.
106 X. Tang, X. Ma, D. Qiu, G. Bu, Y. Xia, B. Zhao, Z. Lin and Y. Shi, *IOP Conf. Ser.:Mater. Sci. Eng.*, 2018, **301**, 012108.
107 B.-L. Yan, D. Jun, J. Wang, T. Yang and X.-H. Mao, *J. Alloys Compd.*, 2022, **905**, 164121.
108 S. K. Park, C. Y. Seong, S. Yoo and Y. Piao, *Energy*, 2016, **99**, 266–273.
109 K. Lv, Y. Zhang, D. Zhang, W. Ren and L. Sun, *J. Mater. Sci.:Mater. Electron.*, 2017, **28**, 14919–14927.
110 J. Chen, Z. Bai, X. Li, Q. Wang, J. Du, R. Lu and X. Liu, *Ceram. Int.*, 2022, **48**, 31923–31930.
111 H. Liu, Z. Hu, H. Ruan, R. Hu, Y. Su, L. Zhang and J. Zhang, *J. Mater. Sci.:Mater. Electron.*, 2016, **27**, 11541–11547.
112 H. Xia, M. Lai and L. Lu, *J. Mater. Chem.*, 2010, **20**, 6896–6902.
113 L. Feng, Z. Xuan, H. Zhao, Y. Bai, J. Guo, C. W. Su and X. Chen, *Nanoscale Res. Lett.*, 2014, **9**, 1–8.
114 N. Li, P. Zheng, R. Wang and X. Zhao, *J. Mater. Sci.:Mater. Electron.*, 2024, **35**, 1504.
115 W. Jian-Gan, in *Supercapacitor Design and Applications*, ed. S. Zoran, IntechOpen, Rijeka, 2016, ch. 3, DOI: 10.5772/65008.
116 D. Wang, Y. Wang, Q. Li, W. Guo, F. Zhang and S. Niu, *J. Power Sources*, 2018, **393**, 186–192.

117 H. Liu, Z. Hu, Y. Su, H. Ruan, R. Hu and L. Zhang, *Appl. Surf. Sci.*, 2017, **392**, 777–784.
118 Z. Ma and T. Zhao, *Electrochim. Acta*, 2016, **201**, 165–171.
119 S. Jamil, S. R. Khan, B. Sultana, M. Hashmi, M. Haroon and M. R. S. A. Janjua, *J. Cluster Sci.*, 2018, **29**, 1099–1106.
120 T. Li, Y. Lan, W. Yang, J. Wang, C. Wang, S. Yao and Y. Wang, *J. Mater. Sci.:Mater. Electron.*, 2024, **35**, 9, DOI: 10.1007/s10854-023-11747-2.
121 H. Liang, H. Xiang, R. Zhu, C. Liu and Y. Jia, *J. Mater. Chem. A*, 2021, **9**, 14566–14575.
122 Z. Li, M. Yang, F. Geng, D. Zhang, Y. Zhang, X. Zhang, X. Pang and L. Geng, *Dalton Trans.*, 2023, **52**, 18194–18205.
123 L. Zhang, J. Xu, X. Hu, K. Song, J. Wu, B. Li and J. P. Cheng, *J. Appl. Electrochem.*, 2019, **49**, 1193–1202.
124 W. Zou, H. Fang, T. Ma, Y. Zhao, L. Wang, X. Jia and L. Zhang, *Batteries*, 2023, **9**, 389.
125 T. B. N. Le, H. T. Lai, T. L. Nguyen, Q. N. Tran, N. Q. M. Tran, L. H. T. Nguyen, T. L. H. Doan, A. T. T. Pham, C. K. Jayasankar, B. Jang, J. Hong and T. B. Phan, *Solid State Sci.*, 2024, **151**, 107504.
126 R. Zhang, D. Wang, L. C. Qin, G. Wen, H. Pan, Y. Zhang, N. Tian, Y. Zhou and X. Huang, *J. Mater. Chem. A*, 2017, **5**, 17001–17011.
127 Y. Pan, M. Xu, L. Yang, M. Yu, H. Liu and F. Zeng, *J. Alloys Compd.*, 2020, **819**, 152969.
128 M. Jing, J. Wang, H. Hou, Y. Yang, Y. Zhang, C. Pan, J. Chen, Y. Zhu and X. Ji, *J. Mater. Chem. A*, 2015, **3**, 16824–16830.
129 X. Cui, Y. Wang, Q. Xu, P. Sun, X. Wang, T. Wei and Y. Sun, *Nanotechnology*, 2017, **28**, 255402.
130 Y. Huang, F. Lai, L. Zhang, H. Lu, Y. E. Miao and T. Liu, *Sci. Rep.*, 2016, **6**, 31541.
131 Y. Meng, Y. Liu, J. He, X. Sun, A. Palmieri, Y. Gu, X. Zheng, Y. Dang, X. Huang, W. Mustain and S. L. Suib, *ACS Appl. Energy Mater.*, 2021, **4**, 5424–5433.
132 X. Zhang, W. Wu, Y. Wang, R. Zhu, T. Yang, X. Li, S. Wang, D. Xiang and Y. Zhang, *JOM*, 2024, **76**, 1192–1202.
133 E. Singh and H. S. Nalwa, *RSC Adv.*, 2015, **5**, 73575–73600.
134 A. K. Geim and K. S. Novoselov, *Nat. Mater.*, 2007, **6**, 183–191.
135 D. Guo, Z. Hu, Q. Li, L. Bian, Y. Song and X. Liu, *J. Mater. Sci.*, 2022, **57**, 563–575.
136 H. Wu, D. He and Y. Wang, *Mater. Lett.*, 2020, **268**, 127613.
137 W. Zhang, X. Guo, J. Zhao, Y. Zheng, H. Xie, Z. Zhang, S. Wang, Q. Xu, Q. Fu and T. Zhang, *J. Electroanal. Chem.*, 2022, **910**, 116170.
138 Q. Zhang, Q. Wang, S. Huang, Y. Jiang, Z. Hu and Z. Chen, *J. Mater. Sci.:Mater. Electron.*, 2021, **32**, 3543–3555.
139 W. Meng, C. Dong, J. Shao, Q. Wang, H. Cheng and H. Gong, *Mater. Sci. Semicond. Process.*, 2022, **145**, 106638.
140 P. Rosaiah, J. Zhu, D. P. Shaik, H. O. M, Y. Qiu and L. Zhao, *J. Electroanal. Chem.*, 2017, **794**, 78–85.
141 W. Li, A. Xu, Y. Zhang, Y. Yu, Z. Liu and Y. Qin, *J. Alloys Compd.*, 2022, **897**, 162640.
142 International Organisation for Standardization, *Nanotechnologies - Vocabulary*, ISO/TS 80004-13:2024, https://www.iso.org/standard/82855.html, (accessed May 2025).
143 X. Huang, Z. Yin, S. Wu, X. Qi, Q. He, Q. Zhang, Q. Yan, F. Boey and H. Zhang, *Small*, 2011, **7**, 1876–1902.
144 Y. Zhu, S. Murali, W. Cai, X. Li, J. W. Suk, J. R. Potts and R. S. Ruoff, *Adv. Mater.*, 2010, **22**, 3906–3924.
145 M. Pumera, *Chem. Soc. Rev.*, 2010, **39**, 4146–4157.
146 K. Spilarewicz-Stanek, A. Kisielewska, J. Ginter, K. Bałuszyńska and I. Piwoński, *RSC Adv.*, 2016, **6**, 60056–60067.
147 L. Fan, Y. Zhang, Z. Guo, B. Sun, D. Tian, Y. Feng, N. Zhang and K. Sun, *Chemistry*, 2020, **26**, 9314–9318.
148 G. Li, Z. Li, Z. Hou, Y. Liu and S. Jiao, *Electrochim. Acta*, 2020, **363**, 137184.
149 K. An, J. He, L. Yang, L. Shen and Y. Sun, *Int. J. Energy Res.*, 2020, **44**, 12180–12187.
150 X. Zhao, H. Yang, Y. Hou, L. Gbologah, L. Zhu and Y. Wang, *Prog. Nat. Sci.: Mater. Int.*, 2019, **29**, 504–510.
151 M. Jayashree, M. Parthibavarman, R. BoopathiRaja, S. Prabhu and R. Ramesh, *J. Mater. Sci.: Mater. Electron.*, 2020, **31**, 6910–6918.
152 A. Romaní Vázquez, C. Neumann, M. Borrelli, H. Shi, M. Kluge, W. Abdel-Haq, M. R. Lohe, C. Gröber, A. Röpert, A. Turchanin, S. Yang, A. Shaygan Nia and X. Feng, *Nanoscale*, 2021, **13**, 15859–15868.
153 G. Mustafa, G. Mehboob, S. N. Khisro, M. Javed, X. Chen, M. S. Ahmed, J. M. Ashfaq, G. Asghar, S. Hussain, A. U. Rashid and G. Mehboob, *Front. Chem.*, 2021, **9**, 717074.
154 Y. Li, L. Tang, D. Deng, H. He, X. Yan, J. Wang and L. Luo, *Mater. Sci. Eng., C*, 2021, **118**, 111443.
155 Abid, P. Sehrawat, S. S. Islam, P. Mishra and S. Ahmad, *Sci. Rep.*, 2018, **8**, 3537.
156 M. H. Fahmy Taha, H. Ashraf and W. Caesarendra, *Appl. Syst. Innov.*, 2020, **3**, 32.
157 P. Montes-Navajas, N. G. Asenjo, R. Santamaría, R. Menéndez, A. Corma and H. García, *Langmuir*, 2013, **29**, 13443–13448.
158 M. Khan, M. N. Tahir, S. F. Adil, H. U. Khan, M. R. H. Siddiqui, A. A. Al-warthan and W. Tremel, *J. Mater. Chem. A*, 2015, **3**, 18753–18808.
159 V. Singh, D. Joung, L. Zhai, S. Das, S. I. Khondaker and S. Seal, *Prog. Mater. Sci.*, 2011, **56**, 1178–1271.
160 Y. Chen, X. Zhang, D. Zhang, P. Yu and Y. Ma, *Carbon*, 2011, **49**, 573–580.
161 Y. S. Yun, G. Yoon, M. Park, S. Y. Cho, H.-D. Lim, H. Kim, Y. W. Park, B. H. Kim, K. Kang and H.-J. Jin, *NPG Asia Mater.*, 2016, **8**, e338.
162 A. Benchirouf, C. Muller and O. Kanoun, *Nanoscale Res. Lett.*, 2016, **11**, 4.
163 W. Chen, L. Yan and P. R. Bangal, *J. Phys. Chem. C*, 2010, **114**, 19885–19890.

164 M. Goumri, B. Lucas, B. Ratier and M. Baitoul, *Opt. Mater.*, 2016, **60**, 105–113.
165 S. Gilje, S. Han, M. Wang, K. L. Wang and R. B. Kaner, *Nano Lett.*, 2007, **7**, 3394–3398.
166 Y. Zhao, J. Liu, B. Wang, J. Sha, Y. Li, D. Zheng, M. Amjadipour, J. MacLeod and N. Motta, *ACS Appl. Mater. Interfaces*, 2017, **9**, 22588–22596.
167 K. Ojha, B. Kumar and A. K. Ganguli, *J. Chem. Sci.*, 2017, **129**, 397–404.
168 Q. Ke, Y. Liu, H. Liu, Y. Zhang, Y. Hu and J. Wang, *RSC Adv.*, 2014, **4**, 26398–26406.
169 V. M. Vimuna, A. R. Athira, K. V. Dinesh Babu and T. S. Xavier, *Diamond Relat. Mater.*, 2020, **110**, 108129.
170 X. Li, X. Xu, F. Xia, L. Bu, H. Qiu, M. Chen, L. Zhang and J. Gao, *Electrochim. Acta*, 2014, **130**, 305–313.
171 M. C. Nwankwo, B. Ezealigo, A. C. Nwanya, A. C. Nkele, A. Agbogu, U. Chime, P. U. Asogwa, B. A. Ezekoye, A. B. C. Ekwealor, R. U. Osuji, P. M. Ejikeme, M. Maaza and F. I. Ezema, *Inorg. Chem. Commun.*, 2020, **119**, 107983.
172 J. Mao, F.-F. Wu, W.-H. Shi, W.-X. Liu, X.-L. Xu, G.-F. Cai, Y.-W. Li and X.-H. Cao, *Chin. J. Polym. Sci.*, 2019, **38**, 514–521.
173 S. K. Abdel-Aal, S. Y. Attia and S. G. Mohamed, *J. Electron. Mater.*, 2019, **48**, 4977–4986.
174 A. Kozawa, K. Yamamoto and M. Yoshio, in *Handbook of Battery Materials*, ed. C. Daniel and J. O. Besenhard, Wiley-VCH, Weinheim, 2nd edn, 2011, ch. 4, pp. 125–148.
175 X. Zhu, P. Zhang, S. Xu, X. Yan and Q. Xue, *ACS Appl. Mater. Interfaces*, 2014, **6**, 11665–11674.
176 L. Zhu, F. Scheiba, V. Trouillet, M. Georgian, Q. Fu, A. Sarapulpva, F. Sigel, W. Hua and H. Ehrenberg, *ACS Appl. Energy Mater.*, 2019, **2**, 7121–7131.
177 Z. Huang, Y. Duan, Q. Jing, M. Sun, B. Tang and S. Shi, *J. Alloys Compd.*, 2021, **864**, 158316.
178 J.-R. Sun, D.-S. Li, S.-X. Wang, J.-W. Xu, W.-L. Liu, M.-M. Ren, F.-G. Kong, S.-J. Wang and L.-F. Yang, *J. Alloys Compd.*, 2021, **867**, 159034.
179 F. Jing, Z. Ma, J. Wang, Y. Fan, X. Qin and G. Shao, *Chem. Eng. J.*, 2022, **435**, 135103.
180 Q. Su, S. Wang, G. Du, B. Xu, S. Ma and L. Shang, *J. Phys. Chem. C*, 2018, **122**, 2475–2480.
181 L. Wang, L. Li, H. Wang, J. Yang, F. Wu and R. Chen, *ACS Appl. Energy Mater.*, 2019, **2**, 5206–5213.
182 A. K. Stephan, *Joule*, 2021, **5**, 1–2.
183 I. Hasa, S. Passerini, K. Edstrom, P. Stevens, A. Romanello, R. Scipioni and E. Sheridan, *Transp. Res. Proc.*, 2023, **72**, 3625–3632.
184 Y.-K. Sun, *ACS Energy Lett.*, 2021, **6**, 2187–2189.
185 M. Ryu, Y. K. Hong, S. Y. Lee and J. H. Park, *Nat. Commun.*, 2023, **14**, 1316.